Shear wave velocities in the Pampean flat-slab region from Rayleigh wave tomography: Implications for slab and upper mantle hydration

Ryan Porter,[1,2] Hersh Gilbert,[3] George Zandt,[1] Susan Beck,[1] Linda Warren,[4] Josh Calkins,[5] Patricia Alvarado,[6,7] and Megan Anderson[8]

Received 30 March 2012; revised 19 September 2012; accepted 23 September 2012; published 3 November 2012.

[1] The Pampean flat-slab region, located in central Argentina and Chile between 29° and 34°S, is considered a modern analog for Laramide flat-slab subduction within western North America. Regionally, flat-slab subduction is characterized by the Nazca slab descending to ~100 km depth, flattening out for ~300 km laterally before resuming a more "normal" angle of subduction. Flat-slab subduction correlates spatially with the track of the Juan Fernandez Ridge, and is associated with the inboard migration of deformation and the cessation of volcanism within the region. To better understand flat-slab subduction we combine ambient-noise tomography and earthquake-generated surface wave measurements to calculate a regional 3D shear velocity model for the region. Shear wave velocity variations largely relate to changes in lithology within the crust, with basins and bedrock exposures clearly defined as low- and high-velocity regions, respectively. We argue that subduction-related hydration plays a significant role in controlling shear wave velocities within the upper mantle. In the southern part of the study area, where normal-angle subduction is occurring, the slab is visible as a high-velocity body with a low-velocity mantle wedge above it, extending eastward from the active arc. Where flat-slab subduction is occurring, slab velocities increase to the east while velocities in the overlying lithosphere decrease, consistent with the slab dewatering and gradually hydrating the overlying mantle. The hydration of the slab may be contributing to the excess buoyancy of the subducting oceanic lithosphere, helping to drive flat-slab subduction.

Citation: Porter, R., H. Gilbert, G. Zandt, S. Beck, L. Warren, J. Calkins, P. Alvarado, and M. Anderson (2012), Shear wave velocities in the Pampean flat-slab region from Rayleigh wave tomography: Implications for slab and upper mantle hydration, *J. Geophys. Res.*, *117*, B11301, doi:10.1029/2012JB009350.

1. Introduction

[2] From 8°N to 47°S, the Andean Cordillera is formed by processes related to the subduction of the Nazca plate beneath the South American plate. While the Andean Cordillera is often considered a 'typical' compressive upper plate style subduction zone, there are several along-strike variations in the nature of subduction and the style of deformation. Adjacent to the track of the Juan Fernandez Ridge, between 29° and 32°S [*Yáñez et al.*, 2001], the downgoing Nazca plate flattens for ~300 km before resuming a more typical angle of subduction (Figure 1) [*Cahill and Isacks*, 1992; *Anderson et al.*, 2007]. This unusual slab geometry, known as flat-slab subduction, has led to a shutoff of arc volcanism and a migration of deformation inboard from the high Cordillera into the Sierras Pampeanas in Argentina [*Jordan et al.*, 1983; *Kay et al.*, 1988].

[3] Flat-slab, or low-angle, subduction occurs in approximately 10% of subduction zones on Earth and is associated with the widening, inboard migration, and/or cessation of arc related volcanism [*Cahill and Isacks*, 1992; *Gutscher et al.*, 2000a]. Understanding the driving forces and deformation associated with flat-slab subduction has implications regarding general subduction processes, as well as the tectonic evolution of the western USA, which is believed to have experienced flat-slab subduction during the Laramide orogeny [e.g., *Coney*

[1]Department of Geosciences, University of Arizona, Tucson, Arizona, USA.
[2]Now at Department of Terrestrial Magnetism, Carnegie Institute of Washington, Washington, D. C., USA.
[3]Department of Earth, Atmospheric, and Planetary Sciences, Purdue University, West Lafayette, Indiana, USA.
[4]Department of Earth and Atmospheric Sciences, Saint Louis University, Saint Louis, Missouri, USA.
[5]Lamont-Doherty Earth Observatory, Columbia University, Palisades, New York, USA.
[6]Departamento de Geofisica y Astronomia, Universidad Nacional de San Juan, San Juan, Argentina.
[7]CONICET, San Juan, Argentina.
[8]Department of Geology, Colorado College, Colorado Springs, Colorado, USA.

Corresponding author: R. Porter, Department of Terrestrial Magnetism, Carnegie Institute of Washington, 5241 Broad Branch Rd., NW, Washington, DC 20015-1305, USA. (rporter@dtm.ciw.edu)

0148-0227/12/2012JB009350

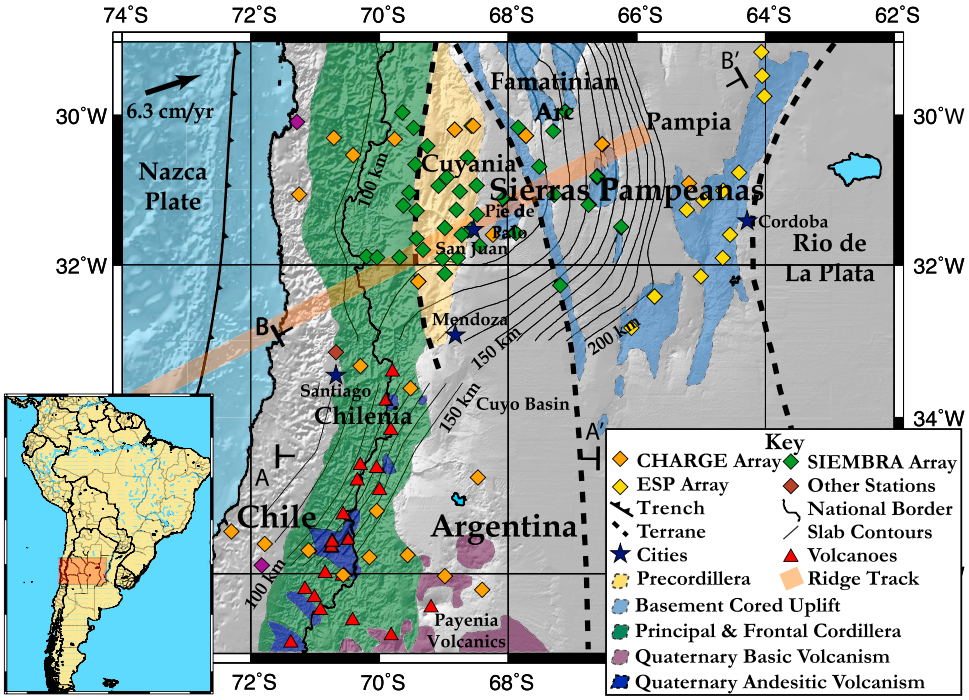

Figure 1. Map of study area showing station locations for each seismic array, active volcanoes, Quaternary volcanism, the track of the Juan Fernandez Ridge [*Yáñez et al.*, 2001], deformational regions and terrane boundaries. The slab contour interval is 10 km; the 100, 150 and 200 km contours are labeled. Northern slab contours are from Linkimer et al. (manuscript in preparation, 2011) and the southern slab contours are from *Anderson et al.* [2007]. The deformational and Quaternary volcanism boundaries are from *Alvarado et al.* [2007] which is based on *Kay and Mpodozis* [2001], *Ramos et al.* [2002], *Bissig et al.* [2002], *Ramos* [2004], and *Stern* [2004]. Cross sections A-A′ and B-B′ are shown in Figures 13 and 14, respectively. Plate convergence velocity from *Kendrick et al.* [2003]. Inset shows the study area location.

and Reynolds, 1977; *Dickinson and Snyder*, 1978]. Several potential causes of flat-slab subduction have been proposed though no single driving force has yet been identified [e.g., *Gutscher et al.*, 2000b]. Some proposed driving mechanisms are slab suction, overthrusting of the overriding plate and increased buoyancy of the subducting slab [e.g., *Jischke*, 1975; *Cross and Pilger*, 1982; *van Hunen et al.*, 2004]. Increased buoyancy of the subducting oceanic plate has been explained by the subduction of young/warm oceanic lithosphere, overthickened oceanic crust related to seamounts or oceanic plateaus, a delay in the basalt to eclogite phase change, and serpentinization of the subducting slab mantle [*Vlaar and Wortel*, 1976; *Sacks*, 1983; *Gutscher et al.*, 2000b; *Kopp et al.*, 2004; *Gans et al.*, 2011].

[4] Within the study area, the flattest subduction correlates spatially with the subduction of the Juan Fernandez Ridge, a chain of seamounts formed offshore due to volcanism associated with the Juan Fernandez hot spot, suggesting that the two are related. Plate reconstructions suggest a northward bend in the track of the Juan Fernandez Ridge beneath the eastern Sierras Pampeanas [*Pilger*, 1981; *Yáñez et al.*, 2002]. These models also indicate that the ridge previously subducted beneath South America to the north of its current position and has migrated southward to its current location. Geochemical observations of arc volcanics suggest that the slab began shallowing at ~16 Ma when the ridge first migrated into the area and that it assumed its current geometry by ~2 Ma when arc related volcanism ceased [*Kay and Mpodozis*, 2002]. Two specific mechanisms for increased slab buoyancy associated with ridge subduction are (a) volcanism associated with ridge formation thickening the oceanic crust and (b) hydration of the oceanic crust and upper mantle due to the infiltration of water along the ridge reducing the density of the subducting oceanic lithosphere [e.g., *Yáñez et al.*, 2002; *Kopp et al.*, 2004; *Gans et al.*, 2011].

[5] For this study we use Rayleigh-wave tomography, calculated from both ambient noise and earthquake-generated surface waves, to create a regional 3D model of shear wave velocities in order to better understand flat-slab subduction. We focus on analyzing the forces potentially driving flat-slab subduction as well as its effects on crustal and upper-mantle structure and processes. This is done through a comparison of shear wave velocity features observed in the flat-slab subduction region to shear wave velocities in the normal-angle subduction region located immediately to the south. The combination of ambient noise and earthquake-generated surface wave measurements allow for the study of the region at greater depth ranges and detail than would be possible with either method individually.

2. Tectonic Setting

[6] From 29° to 33°S, regional seismicity shows the subducting Nazca plate descending to ~100 km depth, flattening out and remaining at a constant depth for ~300 km laterally before returning to a more normal subduction angle (Figure 1)

[*Cahill and Isacks*, 1992; *Anderson et al.*, 2007; *Gans et al.*, 2011; L. Linkimer et al., Appendix C: Geometry of the Wadati-Benioff Zone and deformation of the subducting Nazca Plate in the Pampean Flat slab of west-central Argentina Lithospheric structure of Pampean flat slab (Latitude 30–33°S) and northern Costa Rica (Latitude 9–11°N) subduction zones, manuscript in preparation, 2011]. The onset of flat-slab subduction led to the eastward migration and diminution of volcanism within the study area from 16 Ma until cessation at 2 Ma [*Kay and Mpodozis*, 2002]. This migration and lessening of volcanism is associated with a shutoff of corner flow in the area where the slab actively dewaters, and thereby prevents the temperature/pressure/hydration conditions necessary for arc volcanism. Along with the shut-off of arc-related volcanism, flat-slab subduction is also associated with increased crustal seismicity [*Gutscher*, 2002; *Alvarado et al.*, 2007, 2009] and at least temporally with the migration of deformation inboard from the high Andes into the thin-skinned Precordillera and thick-skinned Sierras Pampeanas [*Ramos et al.*, 2002].

[7] Flat-slab subduction correlates spatially with the track of the Juan Fernandez Ridge. Volcanism along the ridge, associated with the Juan Fernandez hot spot, is believed to result in moderately overthickened oceanic crust observed where the slab is horizontal, possibly providing some of the buoyancy necessary to maintain flat-slab subduction [*Gans et al.*, 2011]. Active source seismic work [*Kopp et al.*, 2004] and outer rise aftershock locations [*Fromm et al.*, 2006] provide substantial evidence that the slab is significantly fractured and hydrated as a result of this volcanism and outer rise related extension. However, work by *Wagner et al.* [2005, 2006], suggests that the lithosphere above the subducting slab is dry. These observations imply that the slab is hydrated offshore but not releasing water into the upper mantle above the flat slab.

[8] The crustal rocks within the study area can be subdivided both in terms of style of deformation and terrane inheritance. Terrane accretions young to the west but the precise locations of many of their boundaries, which are difficult to determine where not defined by exposed ophiolite belts, are still relatively uncertain. In the following section we briefly outline regional deformation patterns and the terrane geology of the area.

[9] The high Andes are divided into the Principal and Frontal Cordillera which both consist of thick- and thin-skinned thrust belts largely covered by volcanic rocks related to the now inactive arc [*Allmendinger et al.*, 1990]. The Principal Cordillera lies to the west of the Frontal Cordillera, though the boundary is difficult to discern due to the aforementioned volcanic cover (Figure 1). The primary difference between these two regions is the age of the basement rocks. The Principal Cordillera is characterized by Mesozoic and Tertiary volcanic rocks and sedimentary strata, while the Frontal Cordillera is composed of late Paleozoic marine and early Mesozoic igneous rocks [*Allmendinger et al.*, 1990]. Both the Principal and Frontal Cordillera lie within the Chilenia terrane, which extends from the high Andes to the plate margin [*Ramos et al.*, 1986]. Little is known about Chilenia due to the dearth of outcrops. Based on the a small number of U-Pb ages calculated by *Ramos and Basei* [1997a, 1997b] (referenced in *Ramos* [2010]) it is argued that parts of Chilenia are covered by sediments derived from the west and that it is possibly a Laurentia derived terrane.

[10] The Precordillera is a thin-skinned fold and thrust belt to the east of the Principal and Frontal Cordillera (Figure 1). It is separated from the high Andes by a north-south striking piggyback basin that is identified at the surface as the Calingasta, Iglesia, and Barreal valleys. The Precordilleran basement is composed primarily of Paleozoic shelf carbonates [*Astini et al.*, 1995] that in balanced cross sections accommodated ~65–70% of the total regional shortening since 10 Ma [*Allmendinger et al.*, 1990]. The Precordillera comprises the western half of the Cuyania terrane; a Laurentia derived composite terrane that formed offshore before accretion onto South America during Middle to Late Ordovician times in the interpretation of *Ramos* [2004]. The rocks within the Cuyania terrane are believed to be of Grenville age [e.g., *Vujovich et al.*, 2004] and derived from the Ouachita embayment [*Thomas and Astini*, 1996, 2003].

[11] The eastern part of the study area consists of the Sierras Pampeanas, a thick-skinned block-faulted belt of deformation that extends ~800 km inboard from the subduction interface. The style of deformation within the Sierras Pampeanas is characterized by large basement-cored uplifts separated by sediment-filled basins (Figure 1) and is often recognized as an analog to Laramide deformation within the western United States [e.g., *Jordan et al.*, 1983; *Jordan and Allmendinger*, 1986]. The Sierras Pampeanas extend from the eastern half of the Cuyania terrane across the Pampean terrane to the edge of the Rio de Plata craton (Figure 1). The most westerly basement cored uplift is Sierra Pie de Palo, which lies directly east of the city of San Juan and is surrounded on all sides by sedimentary basins (Figure 1) [*Vergés et al.*, 2007]. The Pie de Palo basement block makes up the eastern half of the Cuyania composite terrane described previously. The extent of Pampia, its origin and its role in the formation of the Famatinian magmatic arc as well as the Sierras de Córdoba [*Rapela et al.*, 1998] remain enigmatic. Recent work identifies it as a cratonic block that rifted off Rodinia and eventually collided with the Rio de la Plata craton [*Ramos et al.*, 2010].

[12] The portion of the study areas south of 33°S is characterized by normal-angle subduction and an active volcanic arc [*Stern*, 2004; *Anderson et al.*, 2007]. Prior to 5 Ma, a shallow angle of subduction is inferred within the area based on the location of Late Miocene volcanic rocks 500 km inboard from the trench [*Kay et al.*, 2006; *Ramos and Folguera*, 2009]. This was followed by steepening of the slab that led to back-arc extension and volcanism with an intraplate geochemical signature, referred to as the Payenia volcanic province [*Kay et al.*, 2006; *Ramos and Folguera*, 2011]. Our study area encompasses the northern part of this volcanic province, which consists of small isolated volcanoes and lava flows [*Ramos and Folguera*, 2011]. The Cuyo basin, an inverted Triassic rift basin filled with 1,500 to 2,000 m of continental sediments is also located in this area (Figure 1) [*Ramos et al.*, 1991].

3. Data and Methods

[13] Both ambient-noise tomography [*Shapiro et al.*, 2005; *Moschetti et al.*, 2007; *Yang et al.*, 2007] and a two-plane wave approximation of earthquake-generated surface waves [*Forsyth et al.*, 1998; *Forsyth and Li*, 2005] were used to measure Rayleigh wave phase velocities across the region.

Phase velocity dispersion curves from both methods were then combined and inverted to calculate 1D shear wave velocity profiles every 0.1° in latitude and longitude. Rayleigh waves are sensitive to the velocity structure surrounding their path, with the peak sensitivity at a depth of approximately 1/3 of their wavelengths (auxiliary material Figure S1) [*Yang et al.*, 2007].[1] Ambient noise measurements were used to calculate phase velocities at shorter periods (≤30 s), which primarily sample the crust, while the two-plane wave method was used at longer periods (≥20 s), which sample the lower-crust and upper-mantle (auxiliary material Figure S1). As seen in Figure S1, Rayleigh waves in the period range of interest average over a range of depths so velocities across a sharp discontinuity will be averaged together. Rayleigh waves at 100 s period cannot resolve layers within the crust. Despite this, rough estimations of the depths of sharp shear-velocity discontinuities can be made using surface wave tomography. In this study we assume an isotropic velocity structure.

[14] Data used in this work were primarily collected by three temporary seismic arrays, the Chile Argentina Geophysical Experiment (CHARGE), the Sierras Pampeanas Experiment using a Multicomponent Broadband Array (SIEMBRA) and the Eastern Sierras Pampeanas (ESP) experiment. Data from two additional permanent stations, Las Campanas (LCO, GSN station) and Peldehue (PEL, GeoScope station), both located in Chile, were also utilized. The CHARGE deployment consisted of 22 seismic stations deployed from 2000 to 2002 primarily in two east-west running lines that extended from Chile into western Argentina (Figure 1). The SIEMBRA seismic experiment consisted of 40 seismometers that were deployed from 2007 to 2009 in a grid centered on the city of San Juan, Argentina (Figure 1). Four seismometers were moved to new sites during the experiment, as such, 44 seismic stations are used in this work. The ESP experiment consisted of 12 seismometers that collected data from 2008 to 2010 in the area around the Córdoba ranges in the easternmost part of the Sierras Pampeanas (Figure 1).

3.1. Ambient Noise

[15] Ambient-noise tomography is based on the principle that the cross-correlation of background seismic noise recorded at two seismometers approximates the Green's function of seismic waves traveling between the two recorders. While ambient noise has been used to calculate P wave velocities [e.g., *Roux et al.*, 2005], it is generally used to measure Rayleigh waves [e.g., *Shapiro et al.*, 2005; *Yang et al.*, 2007; *Bensen et al.*, 2008]. Due to the geometry of wavefront spreading and their slower rate of attenuation, surface waves have larger amplitudes than body waves, making them easier to identify and measure. Ambient-noise tomography is advantageous over earthquake-generated surface wave tomography in that it does not require earthquakes and measures shorter periods and is therefore sensitive to shallower structures. The primary energy sources for ambient-noise tomography are ocean storms and atmospheric disturbances, which typically have peaks in amplitude at periods of 15 and 7.5 s [*Friedrich et al.*, 1998; *Bensen et al.*, 2007].

[16] We briefly outline the general process for calculating seismic velocities using ambient-noise tomography within this paper, for a more detailed explanation of the data processing refer to *Bensen et al.* [2007]. To calculate seismic velocities from ambient noise, 1 Hz vertical component data were retrieved from the CHARGE, SIEMBRA, ESP and permanent stations archived at the IRIS (Incorporated Research Institutions for Seismology) DMC (Data Management Center). The instrument response was removed from all seismograms and data were cut into 1-day increments. Seismograms from each day were then band-pass filtered from 5 to 150 s and the data were normalized to remove signals resulting from earthquakes or other discrete events. This was done using a running-absolute-mean normalization method [*Bensen et al.*, 2007]. Once normalized, a Fast Fourier Transform (FFT) was used to convert the data into the frequency domain where the data were whitened and cross-correlations were calculated every day for station pairs. These daily station cross-correlations were transformed back in the time domain and stacked into month and then yearlong increments. From these stacked cross-correlations, the signal-to-noise ratio (SNR) was calculated and those inter-station measurements with a SNR less than 15 were discarded. The resulting waveform for each station pair was roughly symmetric, centered on 0 s (auxiliary material Figure S2). The positive and negative times represent the waves traveling in opposite directions along the great circle path between the two stations. Dissymmetry in the waveform would result from an irregular distribution of noise sources around the station. This effect is largely due to storms concentrating in different hemispheres throughout the year. To increase the SNR, the time axis for the negative component was multiplied by −1 and the resulting waveform stacked with the positive time component, essentially folding it over the 0 s time axis and producing the symmetric component.

[17] To calculate Rayleigh wave phase velocities between stations, the stacked symmetrical component of the cross-correlations were filtered over narrow bandwidths and the phase velocities were measured at several periods. Measurements were made at 8, 10, 12, 14, 16, 20, 25, and 30, s periods. Waveforms measured at 6, 35 and 40-s periods generally had low signal-to-noise ratios and were discarded. In the method utilized for measuring ambient noise a station spacing of at least 3 wavelengths is recommended to accurately calculate group velocity, we apply that cutoff to phase velocity as well using the inter-station phase velocity and period to determine the wavelength [*Bensen et al.*, 2007]. Given the relatively small size of the array compared to more common continent wide studies [e.g., *Yang et al.*, 2007; *Bensen et al.*, 2008] there was not enough distance between many of the stations to make measurements at these longer wavelengths. For these reasons, we only included ambient noise phase velocity measurements made at periods between 8 and 30 s in the inversion for shear wave velocities.

[18] Using the method outlined in *Barmin et al.* [2001], we calculated phase velocity maps for the study area at each period listed above. This is done by combining phase velocities along inter-station paths to determine dispersion curves at defined grid points (Figure 2). In this step, we experimented with grid spacing ranging from 0.5° to 0.1° and a variety of different damping parameters. Given the dense station spacing, grid points located every 0.1° produced detailed results that did not appear to introduce artificial error into the inversion. Ultimately the values $\alpha = 300$,

[1] Auxiliary materials are available in the HTML. doi:10.1029/2012JB009350.

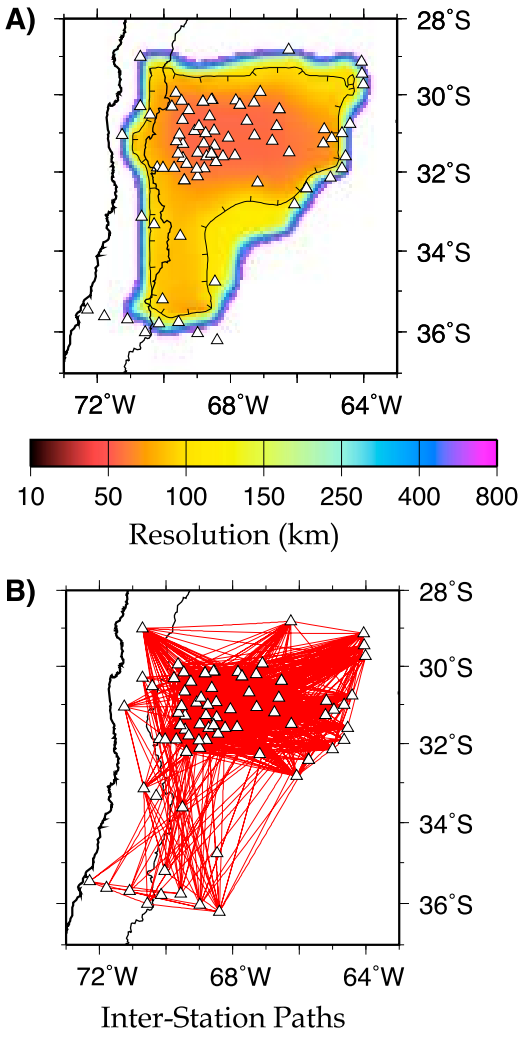

Figure 2. (a) Resolution map for ambient noise phase velocity measurements at the 16 s period. Black line with tickmarks is the 100 km resolution contour. (b) Inter-station paths used at 16 s to calculated phase velocity maps. White triangles are station locations (see Figure 1).

β = 100, and σ = 100 were used in the penalty (damping) function to best match earthquake-generated surface wave measurements. The damping is dependent on the path density with the variable α controlling the strength of the spatial smoothing, β controlling how data is merged into areas of poor data coverage and σ is the smoothing length in km. For a more detailed description of the penalty functions refer to *Barmin et al.* [2001]. As a final quality control on the data, station pairs with residuals greater than 2 s were removed and resolution maps were made (Figure 2). Phase velocity measurements in areas with resolution lengths greater than 100 km were not included in the final inversion for shear wave velocity. Resolution can be interpreted as the minimum distance at which two δ-shaped functions can be resolved [*Barmin et al.*, 2001]. During this step, we also tested the possibility that seasonal biases in noise sources could introduce significant errors into the phase velocity measurements. Phase velocity maps made from noise recorded during the winter months (May to August) were compared to maps made from noise recorded during the summer (November to February) and the two did not exhibit any significant variations in velocity patterns (auxiliary material Figure S3).

3.2. Earthquake-Generated Surface Waves

[19] To calculate Rayleigh wave phase velocities at longer period (≥20 s) we used a two-plane wave approximation of incoming earthquake-generated surface waves [*Forsyth et al.*, 1998; *Forsyth and Li*, 2005]. In this technique, an incoming surface wavefield is approximated as the sum of two interfering plane waves using an iterative two-step inversion. The advantage of this method over single-plane wave approximations is that it is able to account for some of the effects of scattering and multipathing on surface wave velocity calculations. The two-plane wave method has been successfully applied in a variety of seismic studies around the globe. For this study, 94 events were selected with epicenters located 30° to 120° distant from the study area and magnitudes greater than 5.5 (auxiliary material Figure S4). Of these events, 59 occurred during the time SIEMBRA stations were deployed and 35 within the earlier time frame of the CHARGE deployment. Events that occurred solely during the ESP deployment were not used because the array geometry was not conducive to this type of study. The ray coverage from the events used for the 50 s period measurements is shown in auxiliary material Figure S4.

[20] Similar to the ambient-noise analysis, the two-plane wave tomography utilized 1 Hz vertical component seismic records for the 94 events described above. Because the arrays used a variety of instrument types, the instrument responses for all of the stations were transferred to the most common response, that of the Streckeisen STS-2 broadband seismometer, which effectively corrects all data to velocity. Traces were then band-pass filtered using an acausal, 0.01 Hz wide, four-pole, Butterworth filter to make measurements at periods of 20, 22, 25, 27, 30, 34, 40, 45, 50 59, 67, 77, 87 and 100 s. These periods were chosen to accommodate the broadening of depth sensitivity as period increases (auxiliary material Figure S1) and to provide the resolution necessary to observe features in the crust and upper mantle. We are limited to this range of periods by the presence of scattered energy at periods shorter than ~20 s and by a lack of events that generate waves at periods longer than 100 s. Once filtered, the traces were visually windowed around the fundamental Rayleigh wave arrivals and graded based on the quality of the data. Stations with low SNR or where the fundamental-mode Rayleigh wave could not be discerned from higher-mode waves were removed. In preparing the data, anelasticity was accounted for using the attenuation model of *Mitchell* [1995], though studies by *Baumont* [2002] and *Yang and Forsyth* [2008] suggest that the effects of anelasticity are minor.

[21] In the two-plane wave inversion we solve for phase, amplitude and orientation of the two plane waves used to represent the incoming Rayleigh wavefield, for a total of 6 parameters [*Forsyth and Li*, 2005]. While we outline the technique here, a more detailed description can be found in *Forsyth and Li* [2005] and *Yang and Forsyth* [2006]. The inversion involves 8 iterations each with 2 stages. The first stage uses a least squares simulated annealing approach to find the best fitting wave parameters. The second stage is a linearized inversion to calculate corrections to the current velocity model and the wave parameters. In the inversion we

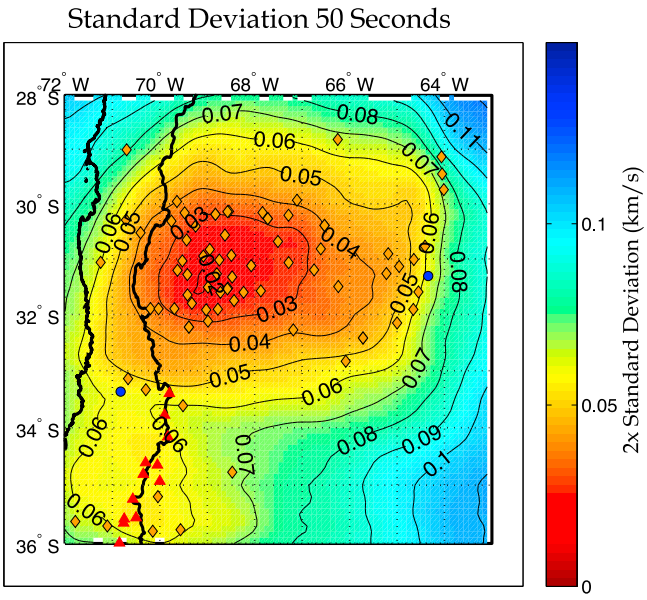

Figure 3. Map of 2× the standard deviation for phase velocity measurements at 50-s period. Measurements where 2× the standard deviation value were less than 0.08 km/s were used in the shear velocity inversion. Orange diamonds are station locations, red triangles are volcanoes, and blue circles are major cities.

use the 2D finite-frequency sensitivity kernels described in *Yang and Forsyth* [2006], which are based on the Born approximation of scattering used in *Zhou et al.* [2004]. Applying these kernels allows the inversion to better-fit amplitude data and increases resolution to detect heterogeneities down to the order of one wavelength of the incoming wavefield [*Yang and Forsyth*, 2006]. Incoming wavefields that cannot be well parameterized by two interfering plane waves are down-weighted in each step of the inversion, reducing the effects of any error introduced by those events. For the 2D phase velocity inversion at each period, a grid spacing of 0.5° was used on a rectangular grid with corners at 38°S, 73°W and 25°S, 61°W. The bounds of the grid were chosen to be sufficiently large that the outermost grid nodes could absorb travel time variations that could not be well fit by the two-plane wave approximation. Measurements were smoothed using a Gaussian smoothing filter with a width of 65 km, which was chosen by experimentation to allow for the observation of the shortest wavelength features possible without introducing spatial aliasing. For each period, grid points where the phase velocity measurement possessed a standard deviation value greater than 0.04 km/s were not included in the inversion for shear wave velocities (Figure 3). Once phase velocities were calculated at all of the 0.5° grid points, the resulting velocity grid was then interpolated to 0.1° grid spacing so that the data could be combined with ambient noise measurements.

3.3. Combined Measurements and Shear Velocity Inversion

[22] Both ambient-noise and two-plane wave tomography dispersion data were combined to produce shear velocity models for the region. Combining measurements from the two techniques has been successfully done in a variety of

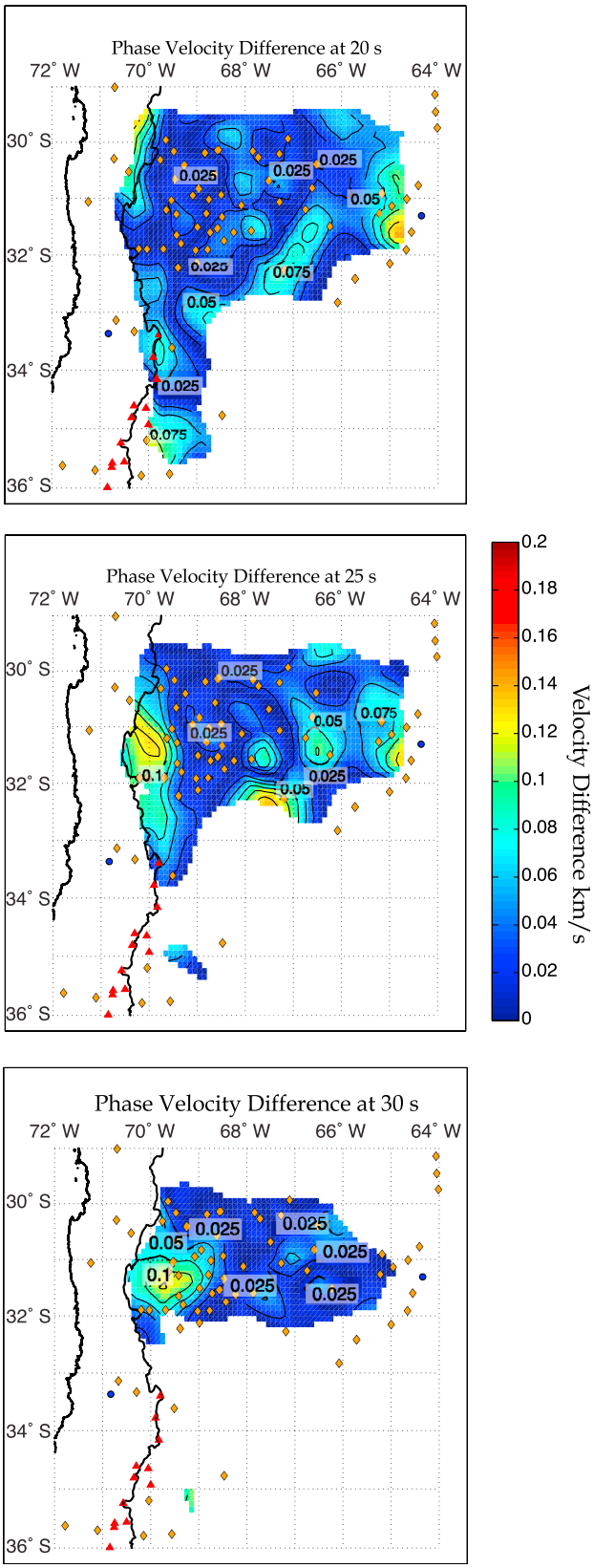

Figure 4. Map of the absolute value of the difference in (top) 20, (middle) 25 and (bottom) 30-s phase velocity measurements between ambient noise and earthquake-generated surface waves at each grid point. Symbols are the same as in Figure 3.

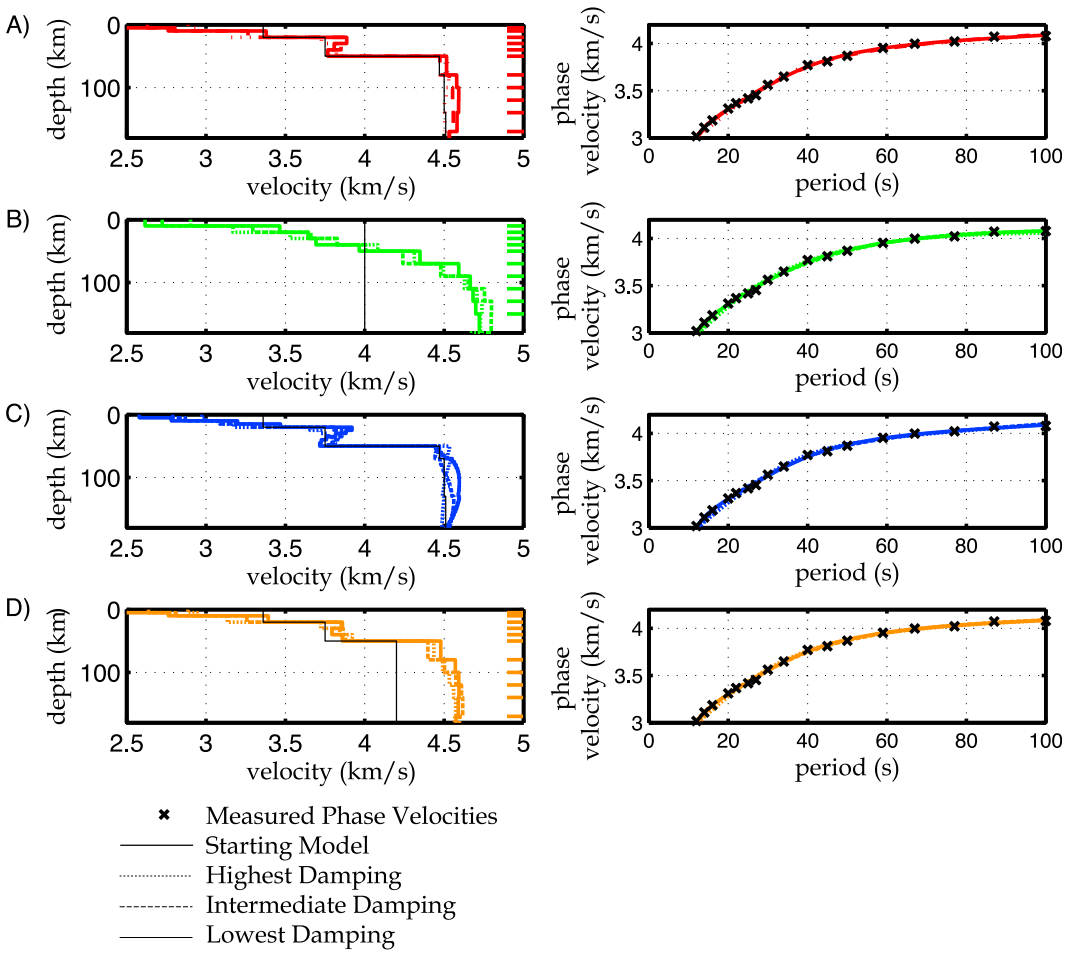

Figure 5. Plots showing the effect of the initial shear velocity model (solid black line), on the inversion results for the grid point at 30.5°S and 68°W. (left) Starting velocity-depth model and inversion results (colored). Colored horizontal lines on the right axis show layer thicknesses used in the inversion for Figures 5a, 5b, and 5d; Figure 5c has 5 km thick layers. (right) Fit to measured phase velocities. (a) Modified IASP91 initial model with variable Moho. (b) Constant initial velocity model. (c) Modified IASP91 initial model with variable Moho and 5 km thick layers. (d) Initial Model with reduced mantle velocity.

studies, and allows for a detailed study of both crust and mantle shear velocities [e.g., *Moschetti et al.*, 2007; *Stachnik et al.*, 2008; *Yang et al.*, 2008]. At every 0.1° × 0.1° grid point, ambient noise and two-plane wave phase velocity measurements were combined into dispersion curves, with ambient noise comprising the short period measurements and two-plane wave tomography comprising the longer period measurements. To evaluate variations in measured phase velocities stemming from the use of the two different techniques, we compared results from overlapping periods where measurements were made using both ambient-noise and two-plane wave tomography (20, 25, and 30 s). Phase velocity results from both methods are consistent and are generally within 0.05 km/s of each other (Figure 4). This is comparable to differences observed by *Yang et al.* [2008]. At overlapping periods, the average of the two velocities was used in the shear velocity inversion where possible. If only one technique met the acceptable resolution/standard deviation criteria described above, then that measurement was used. Grid points without at least four reliable phase velocity measurements were discarded in the shear velocity inversion.

[23] Utilizing the Rayleigh wave peak depth sensitivity for different periods (auxiliary material Figure S1), we inverted phase velocity dispersion curves calculated at each grid point for shear velocities using a linearized least squares inverse method and a constant weight for each input phase velocity [*Herrmann*, 1987; *Snoke and James*, 1997; *Larson et al.*, 2006]. This method was applied using an iterative technique where damping was decreased progressively after 3 to 5 iterations [e.g., *Warren et al.*, 2008]. Figure 5 illustrates the progression of the model through damping parameters and the resulting fit to the dispersion curve. The inversion for shear wave velocity has a large dependence on the starting model, and especially on Moho depth. Given the variable Moho topography within the region [*Fromm et al.*, 2004; *Alvarado et al.*, 2005; *Gilbert et al.*, 2006; *Gans et al.*, 2011], we experimented with a wide variety of initial velocities (Figure 7), before settling on two starting models. The first was a modified IASP91 model [*Kennett and Engdahl*, 1991], where the crustal thickness was varied with longitude to match receiver function measurements [*Gans et al.*, 2011] and the second was a model

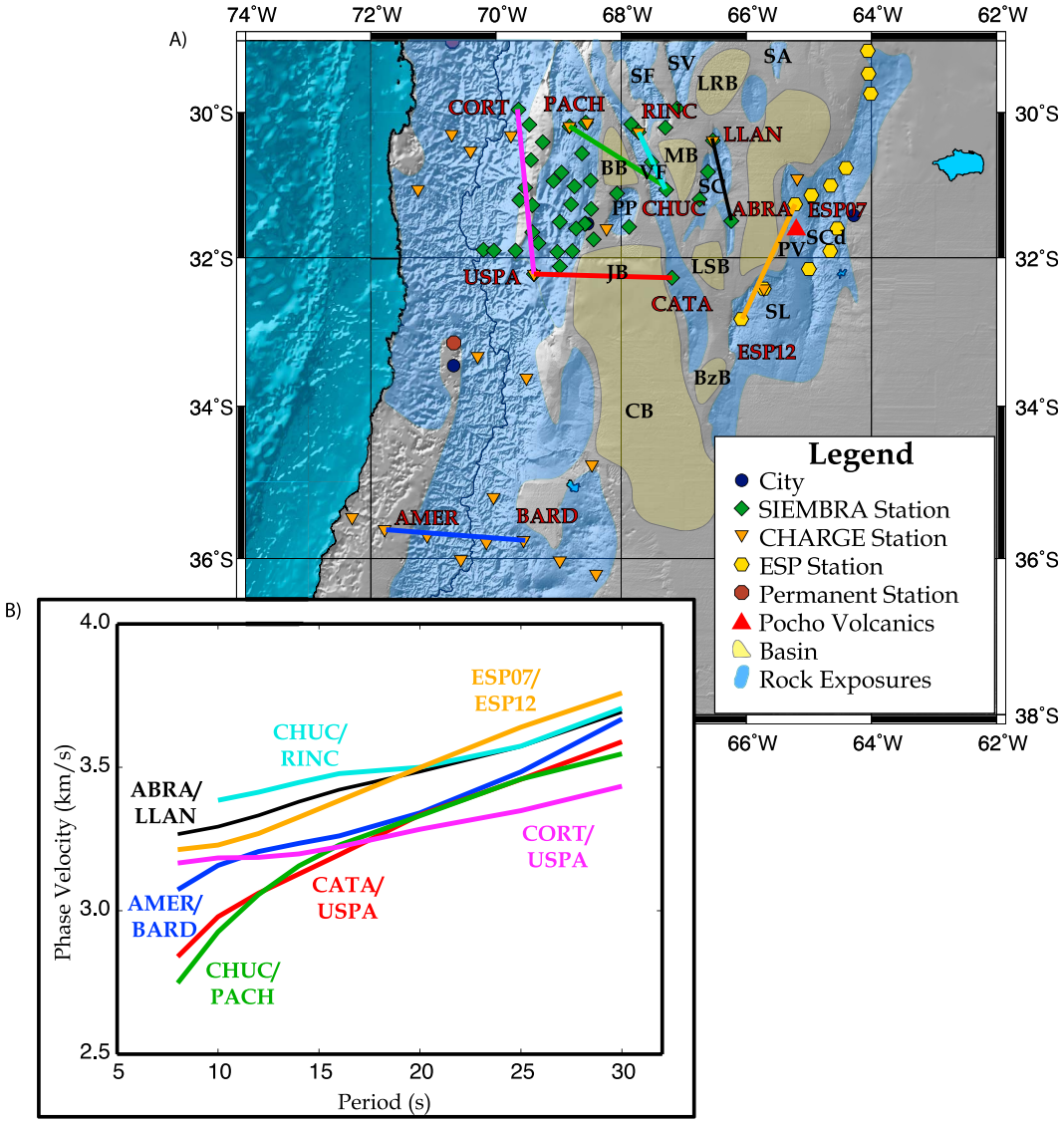

Figure 6. (a) Map of study area showing select inter-station paths overlaid on a map of major basins and bedrock outcrops. Station names are shown in red, bedrock exposures and basins in black. Abbreviations are: BB = Bermejo Basin, BzB = Beazley Basin, CN = Cuyo Basin, JB = Jocoli Basin, LRB = La Rioja Basin LSB = Las Salinas Basin, MB = Marayes Basin, PP = Pie de Palo, PV = Pocho Volcanics, SA = Sierra de Ancasti, SC = Sierras de Chepes, SCd = Sierras de Córdoba, SF = Sierra de Famatina, SL = Sierra de San Luis, SV = Sierra de Velasco VF = Sierra de Valle Fértil. (b) Corresponding dispersion curves for inter-station paths calculated using ambient-noise tomography. Dispersion curve colors correspond to colors on map.

with a constant shear wave velocity of 4 km/s and no Moho (Table 1). In both models the Vp/Vs ratio was kept fixed to the initial value in the inversions (Table 1). We tested the effects of using a variable Vp/Vs (Poisson's) ratio and found that this produced few variations in the final shear velocity model. By comparing results from the two starting models, it is possible to assess the variability of the shear wave velocity features observed in each. In addition to varying the starting velocity model, a variety of layer thicknesses were tested ranging from 5 km thick layers in the crust and mantle to modeling the crust as a single layer. Layer thicknesses less than 20 km in the crust and 30 km in the mantle showed little variations in the final model (Figures 5a and 5c). The final layer thicknesses were selected to observe fine features in the crust and accommodate reduced resolution at depth (Figure 5) (Table 1). Slight variations in layer thicknesses were made across the array in the modified IASP91 model to accommodate the eastward decrease in Moho depth (auxiliary material Figure S5).

4. Results

4.1. Phase Velocities

[24] Using ambient-noise tomography, we calculated inter-station dispersion curves, (Figures 2 and 6), which were then combined to calculate dispersion curves at grid points. These two-station dispersion curves reflect the

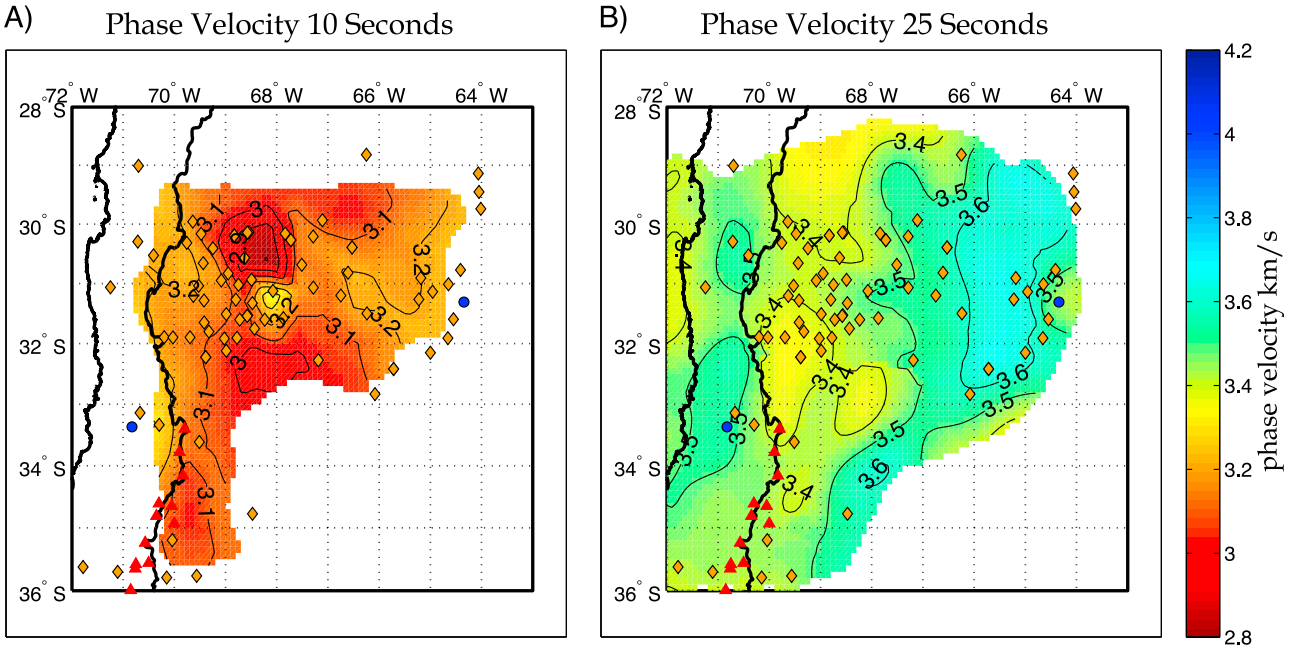

Figure 7. (a) Map of Rayleigh phase velocities measured at 10 s calculated using ambient-noise tomography. The wavelength of a Rayleigh wave with a 10 s period traveling at 3.1 km/s would be 31 km. (b) Map of Rayleigh phase velocities at 25 s calculated by averaging ambient-noise tomography and two-plane wave velocity measurements. The wavelength of a Rayleigh wave with a 25 s period traveling at 3.5 km/s would 88 km. Contour interval is 0.1 km/s. Symbols are the same as in Figure 3.

sensitivity of ambient-noise measurements to upper crustal structure at shorter periods and to crustal thickness at longer periods. The phase velocity measurements made between CHUC and PACH, exhibit low velocities between the 8 and 12 s periods, which reflects the great circle path between the two stations crossing the Bermejo basin, a large 10 km deep foreland basin [*Allmendinger et al.*, 1990; *Gimenez et al.*, 2000] (Figure 6). The dispersion curve calculated between ABRA and LLAN exhibits much higher phase velocities at 8, 10, and 12 s periods, reflecting a station path confined to the bedrock of the Chepes uplift (Figure 6). At longer periods, two higher velocity paths are observed in the eastern half of the study area (e.g., ESP07-ESP12, ABRA-LLAN), compared to the western part (e.g., CORT-USPA, CHUCH-

Table 1. Starting Models for Runs With Defined Moho With 40 km Thick Crust (A in Figure 7) and No Defined Moho (B in Figure 7)[a]

Defined Moho With 40 km Thick Crust						No Defined Moho				
Layer Number	Layer Thickness (km)	P Velocity (km/s)	S Velocity (kms)	Density	1/Q	Layer Thickness (km)	P Velocity (km/s)	S Velocity (kms)	Density	1/Q
1	5.0	5.80	3.36	2.72	0.0017	10.00	7.00	4.00	3.00	0.0018
2	5.0	5.80	3.36	2.72	0.0017	10.00	7.00	4.00	3.00	0.0018
3	10.0	5.80	3.36	2.92	0.0017	10.00	7.00	4.00	3.00	0.0018
4	10.0	6.50	3.75	2.92	0.0017	10.00	7.00	4.00	3.00	0.0018
5	10.0	6.50	3.75	2.92	0.0017	10.00	7.00	4.00	3.00	0.0018
6	20.0	8.04	4.47	3.32	0.0020	20.00	7.00	4.00	3.00	0.0018
7	20.0	8.04	4.47	3.32	0.0020	20.00	7.00	4.00	3.00	0.0018
8	20.0	8.05	4.50	3.37	0.0020	20.00	7.00	4.00	3.00	0.0018
9	20.0	8.05	4.50	3.37	0.0020	20.00	7.00	4.00	3.00	0.0018
10	20.0	8.11	4.50	3.30	0.0020	20.00	7.00	4.00	3.00	0.0018
11	30.0	8.18	4.51	3.43	0.0020	30.00	7.00	4.00	3.00	0.0018
12	30.0	8.18	4.51	3.43	0.0020	30.00	7.00	4.00	3.00	0.0018
13	30.0	8.30	4.52	3.43	0.0020	50.00	7.00	4.00	3.00	0.0018
14	30.0	8.30	4.52	3.43	0.0020	50.00	7.00	4.00	3.00	0.0018
15	30.0	8.50	4.61	3.46	0.0020	100.00	7.00	4.00	3.00	0.0018
16	30.0	8.50	4.61	3.46	0.0020	0.00	7.00	4.00	3.00	0.0018
17	50.0	8.85	4.78	3.52	0.0020					
18	100.0	9.03	4.87	3.54	0.0020					
19	200.0	9.69	5.28	3.88	0.0020					
20	0.0	10.00	5.51	4.00	0.0020					

[a]The number of layers and layer thicknesses were varied in model A to accommodate the eastward decrease in crustal thickness (auxiliary material Figure S5).

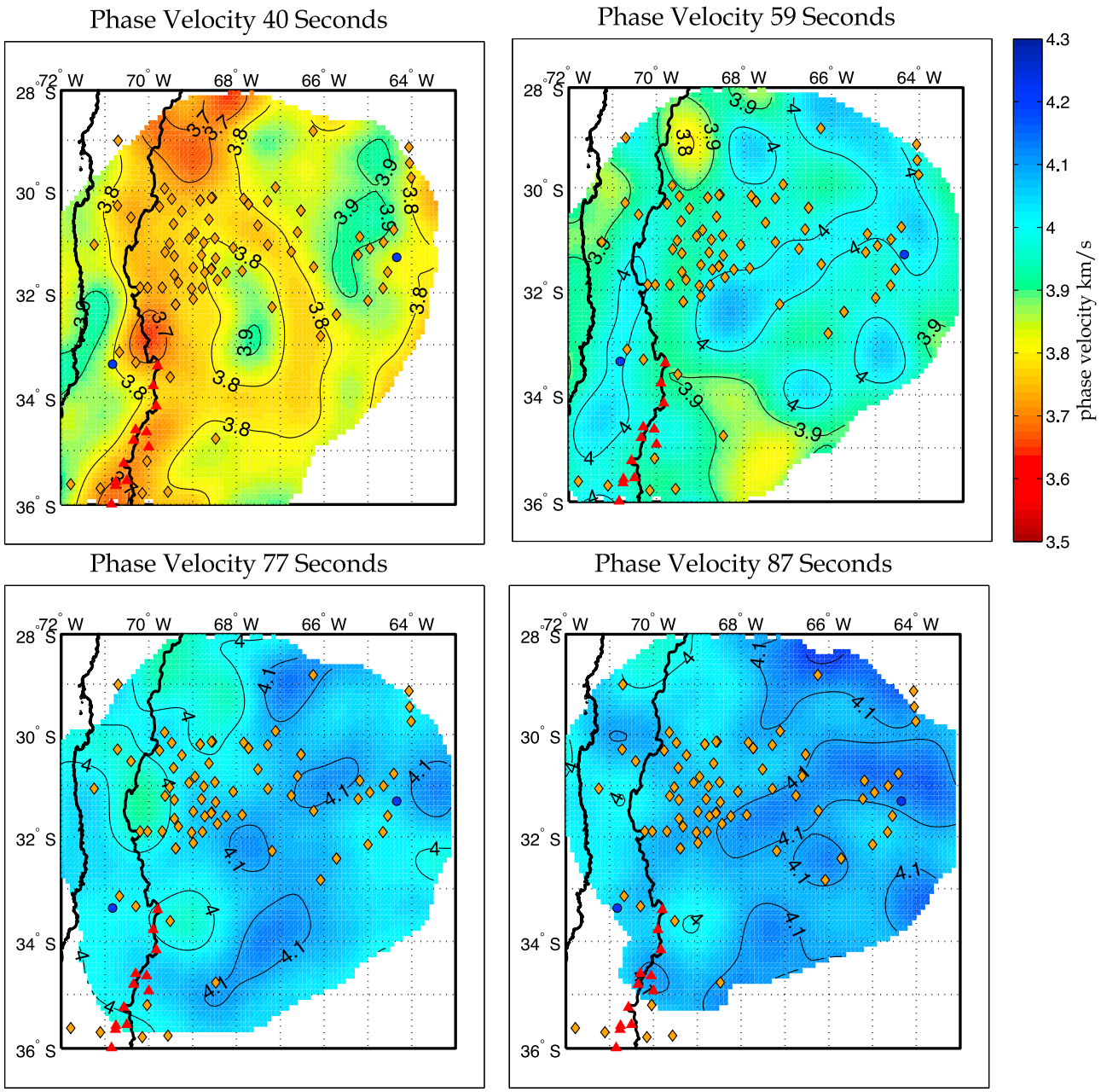

Figure 8. Maps of Rayleigh phase velocities at (top left) 40, (top right) 59, (bottom left) 77, and (bottom right) 87 s, as labeled on plots, calculated using the two-plane wave method. Contour interval is 0.1 km/s. Symbols same as Figure 3.

PACH). These variations likely reflect the thicker crust that is observed in the western half of the study area than in the east [*Fromm et al.*, 2004; *Alvarado et al.*, 2005; *Gilbert et al.*, 2006; *Gans et al.*, 2011]. These inter-station measurements are then combined to produce phase velocity maps (Figure 7), which reflect similar features. Phase velocities calculated at 10 s are lowest in the basins, and higher in locations where bedrock is exposed at the surface (Figure 7). The most prominent features are Sierra Pie de Palo, which exhibits phase velocities >3.3 km/s, and the two foreland basins surrounding it (Figure 7). The Bermejo basin lies to the north and is characterized by phase velocities <2.8 km/s and the Jocoli basin lies to the south and exhibits velocities <3 km/s (Figure 7). The lowest phase velocities observed in the high Andes at the 10 s period are <3.1 km/s, and are found in the southern part of the study area where there is an active arc overlying a region where the Nazca slab subducts at a normal angle, suggesting the presence of magma bodies or partial melt at shallow depths.

[25] Phase velocities calculated at periods of 20, 25 and 30 s are the average of measurements made using both ambient-noise and two-plane wave tomography. Phase velocity maps at these periods show that phase velocities primarily reflect the eastward decrease in crustal thickness (Figure 7), which was previously identified in teleseismic receiver functions, surface waves, and Pn observations [*Fromm et al.*, 2004;

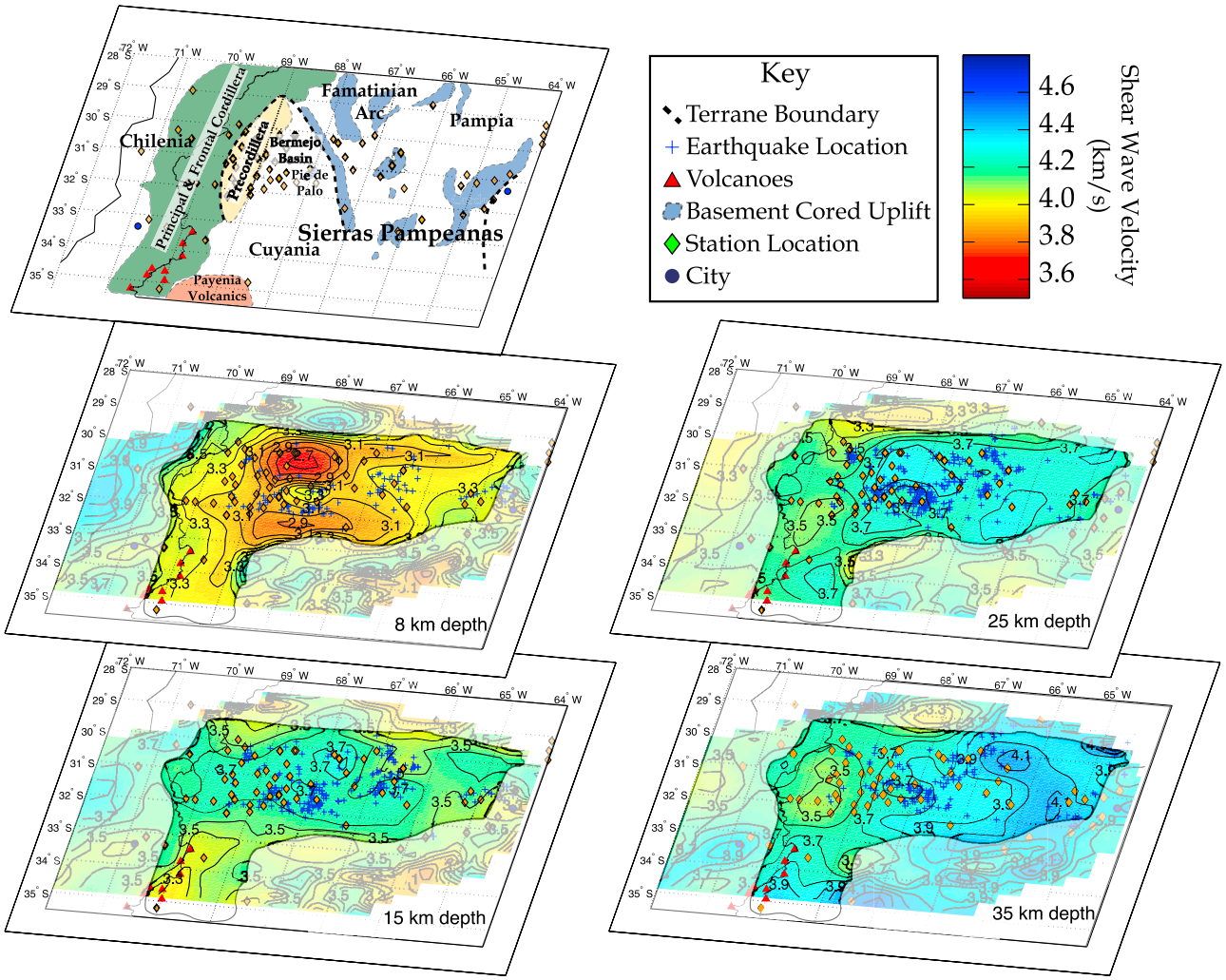

Figure 9. Maps of crustal shear wave velocities calculated at 8, 15, 25 and 35 km depth using a constant shear velocity initial model of 4 km/s. Blue crosses are earthquake locations from Linkimer et al. (manuscript in preparation, 2011) within 10 km of the depth slice. Other symbols are the same as Figure 3. Contour interval is 0.1 km/s. Shaded out area is the region with less than 100 km resolution for phase velocities at 16 s.

Alvarado et al., 2005; *Gilbert et al.*, 2006; *Gans et al.*, 2011]. At 25 s, phase velocities less than 3.4 km/s are observed in the high Cordillera where crustal thicknesses greater than 70 km are observed (Figure 7) [*Gans et al.*, 2011]. In the east beneath the Sierras Pampeanas phase velocities greater than 3.6 km/s are observed suggesting that the Rayleigh waves at this period are partially sampling the upper mantle (Figure 7).

[26] At periods longer than 30 s, measurements were made solely using earthquake-generated surface waves. Maps of phase velocities for periods between 40 and 50 s continue to reflect crustal thickness with higher velocities observed to the east where the crust thins and lower velocities in the zone of thicker crust to the west (Figure 8). From 59 to 87 s, an area of high phase velocity (>4 km/s at 59 s) is observed oriented SW-NE, which possibly marks the location of the subducting slab or dry continental lithosphere immediately above it (Figure 8). At these periods, lower phase velocities are observed where the slab is believed to be flattest (near ~31°S, 68°W), compared to the surrounding area, indicating that the flat slab may have low-velocity features associated with it. At periods greater than 87 s there are few clearly defined phase velocity features and interpretations are more easily made using the results of the shear velocity inversion.

4.2. Shear Velocities

[27] The regional 3D shear velocity model created from the inversion of the phase velocity data is the focus of our interpretation and shows many of the same features observed in the phase velocity measurements. Shear wave velocity maps and cross-sections are shown in Figures 9–12. In both cross-section and map view, we observe a strong correlation in upper crustal seismic velocities and lithology, with bedrock exposures exhibiting higher velocities than sediment filled basins (Figures 9–12). The Bermejo and Jocoli basins are clearly visible at 8 km depth as low-velocity zones (<2.9 km/s) while Sierra Pie de Palo, the Sierras de Chepes, and the Sierras de Córdoba are observed as high-velocity features (>3.1 km/s) (Figure 9). The most notable exception to low velocities associated with basins lies in the area of the active arc to the south where we observe low velocities at

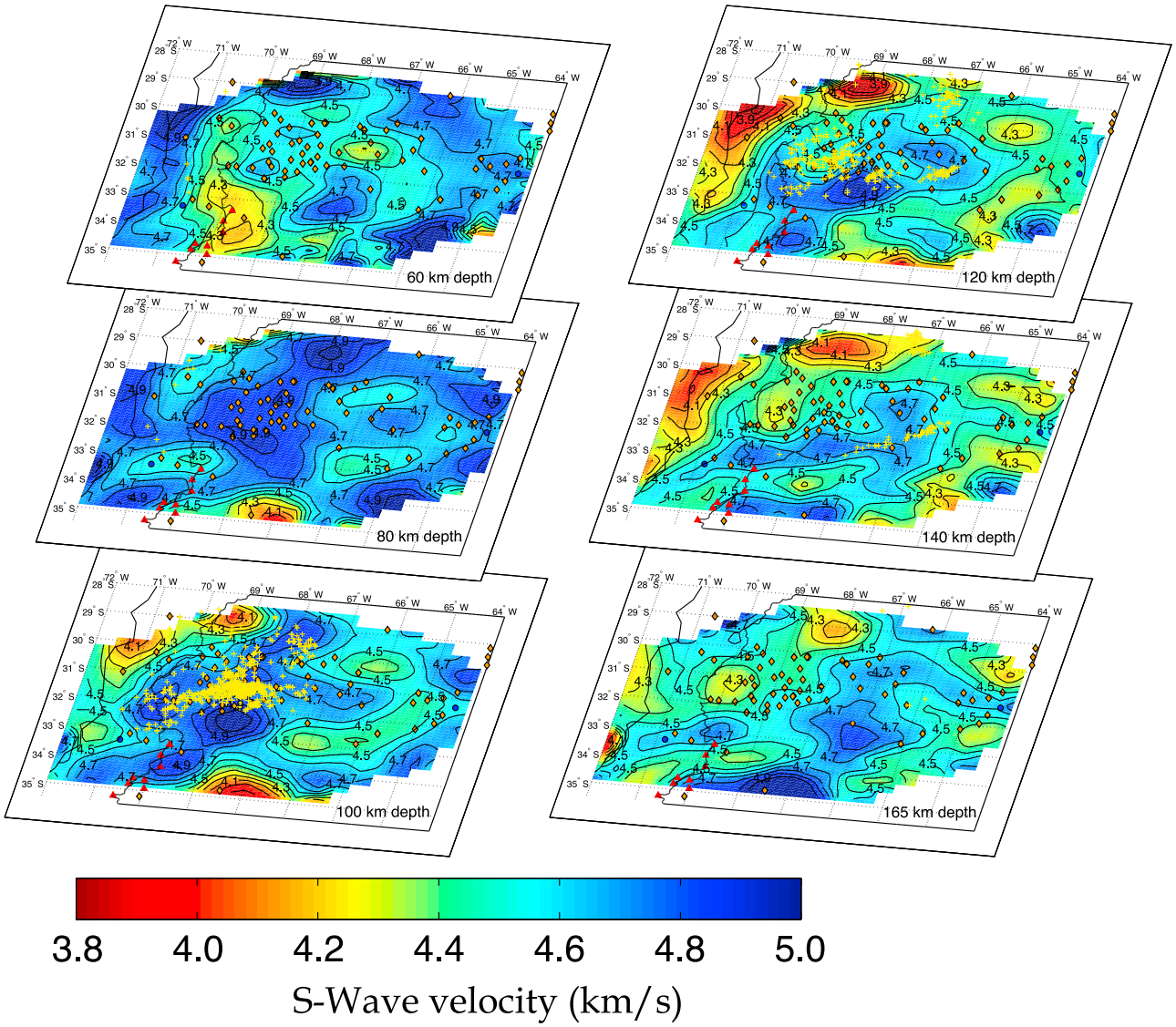

Figure 10. Maps of mantle shear wave velocities calculated at 60, 80, 100, 120, 140 and 165 km depth using a constant shear velocity initial model or 4 km/s. Yellow crosses are earthquake locations from Linkimer et al. (manuscript in preparation, 2011) within 10 km of the depth slice. Other symbols are the same as Figure 3. Contour interval is 0.1 km/s.

15 km depth beneath the arc and recently emplaced volcanic rocks of the Payenia province that lie to the east (Figures 9 and 11). Mid- and lower-crustal velocities are highly dependent on the Moho depth of the starting model. As such, we avoid extensive interpretation of this depth region. The primary observation from the mid crust is that S-wave velocities increase to the east. This observation is most apparent in the north, where the distribution of stations permits E-W variations in velocities to be well resolved (Figure 12). We also observe an increase in Moho depth from east to west across the study area. This trend is observed regardless of starting model and is consistent with prior work measuring regional crustal thicknesses [*Introcaso et al.*, 1992; *Fromm et al.*, 2004; *Alvarado et al.*, 2005; *Gilbert et al.*, 2006; *Gans et al.*, 2011]. Within the upper mantle (Figure 10) we observe significant north-south variations in slab geometry across the region. In the south we observe normal-angle subduction, with a high velocity slab overlying a large low-velocity zone, consistent with asthenosphere emplaced as corner flow (Figure 10). In the north, we image a high-velocity flat slab with pockets of lower velocity material decreasing in volume to the east. This corresponds with an eastward decrease in the velocity of the overlying mantle, consistent with the gradual hydration of this material. A lower velocity region is observed above the slab as it steepens, which is consistent with hydrated mantle material or cool asthenosphere (Figure 10). For the upper mantle SV waves are generally slower than SH waves [*Zhou et al.*, 2006], therefore the inclusion of SH components would likely increase measured shear velocities.

[28] Two cross-sections (Figure 1) were generated to compare the crustal and mantle shear wave velocity features of normal-angle (A-A′) and flat-slab (B-B′) subduction. For each of the cross-section we display results for two different starting models (Figures 11 and 12 and Table 1) to help

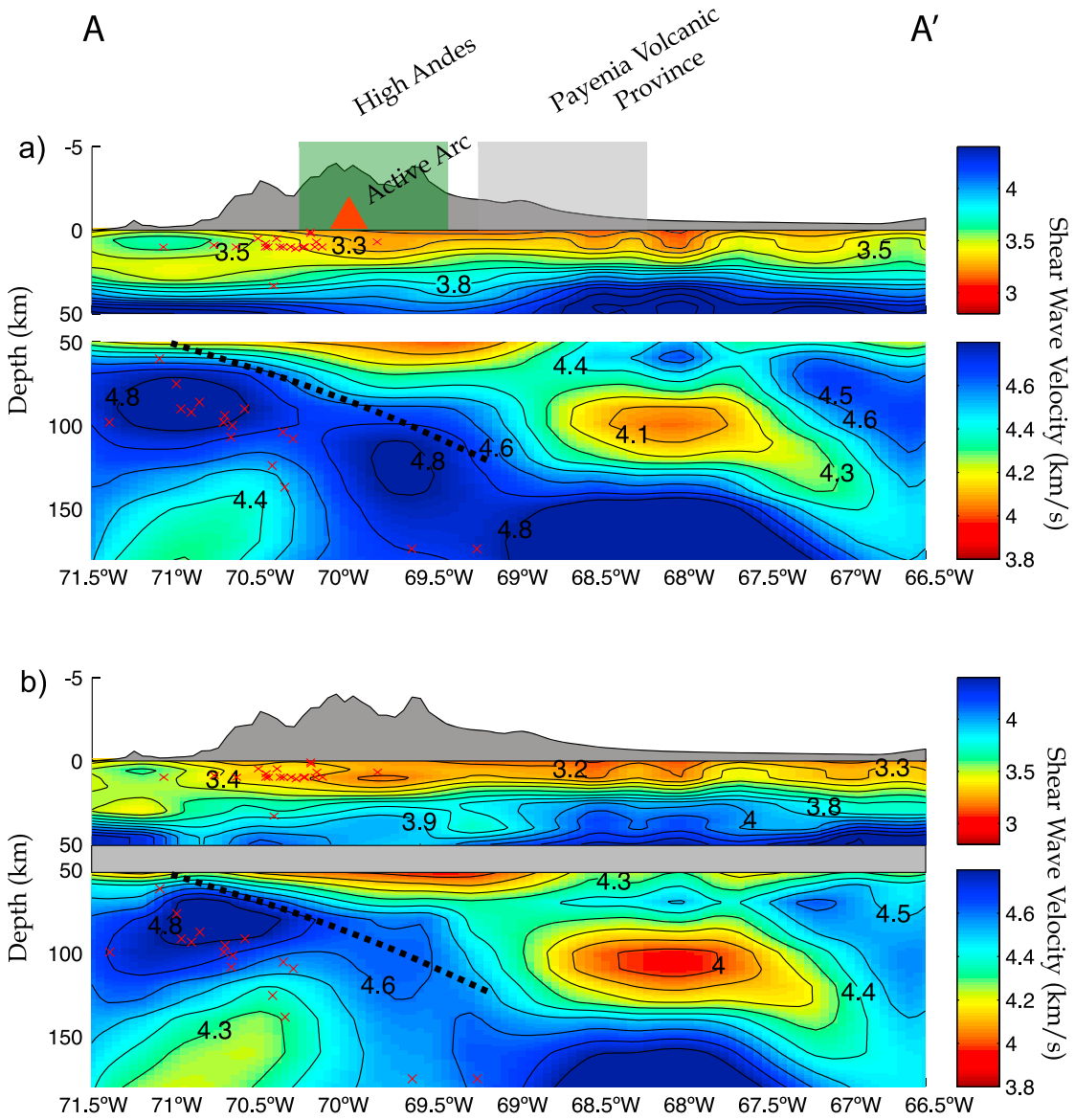

Figure 11. Cross section A-A′ calculated at 34.5°S (see location in Figure 1) using (a) a constant velocity initial model and (b) a variable starting model with a gradational Moho. Contour interval is 0.1 km/s. Red x's are earthquakes locations (mag > 4.0) from the USGS (United States Geological Survey) PDE (Preliminary Determination of Epicenters) catalog from 1973 to 2011 within 0.1 degrees of this vertical slice. Dashed line shows the top of the slab using the utilizing the slab contours from *Anderson et al.* [2007]. Variable smoothing is used to display cross sections in the crust and mantle in order to observe features in each.

illustrate features that are consistent regardless of input model. In both cross-sections we observe high velocity forearcs, crustal roots beneath the high Andes extending down ~70 km, and eastward thinning crust. Beyond these similarities we observe significant variations in the locations and magnitudes of crustal low and high shear-velocity zones. Velocities within the mantle reflect the different subduction geometries observed in the two regions and give insight into the processes occurring in each. Mantle shear velocities in the southern cross-section reflect a more steeply dipping slab with asthenospheric corner flow and an active arc while those in the north are consistent with flat-slab subduction, a shut-off of corner flow and an absence of volcanism. We describe the two cross-sections in detail below.

[29] Cross-section A-A′ in Figure 11, runs east-west and is located at 34.5°S, which is near our southern limit of acceptable resolution (Figure 1). At this latitude, the slab is subducting at a normal angle [*Cahill and Isacks*, 1992; *Fuenzalida et al.*, 1992; *Anderson et al.*, 2007] and there is an active arc associated with it. While the number of crossing raypaths in this area is low relative to the north, it is possible to discern features that are consistent when using either initial model during the shear wave velocity inversion and we focus our interpretation on those. In the cross-section,

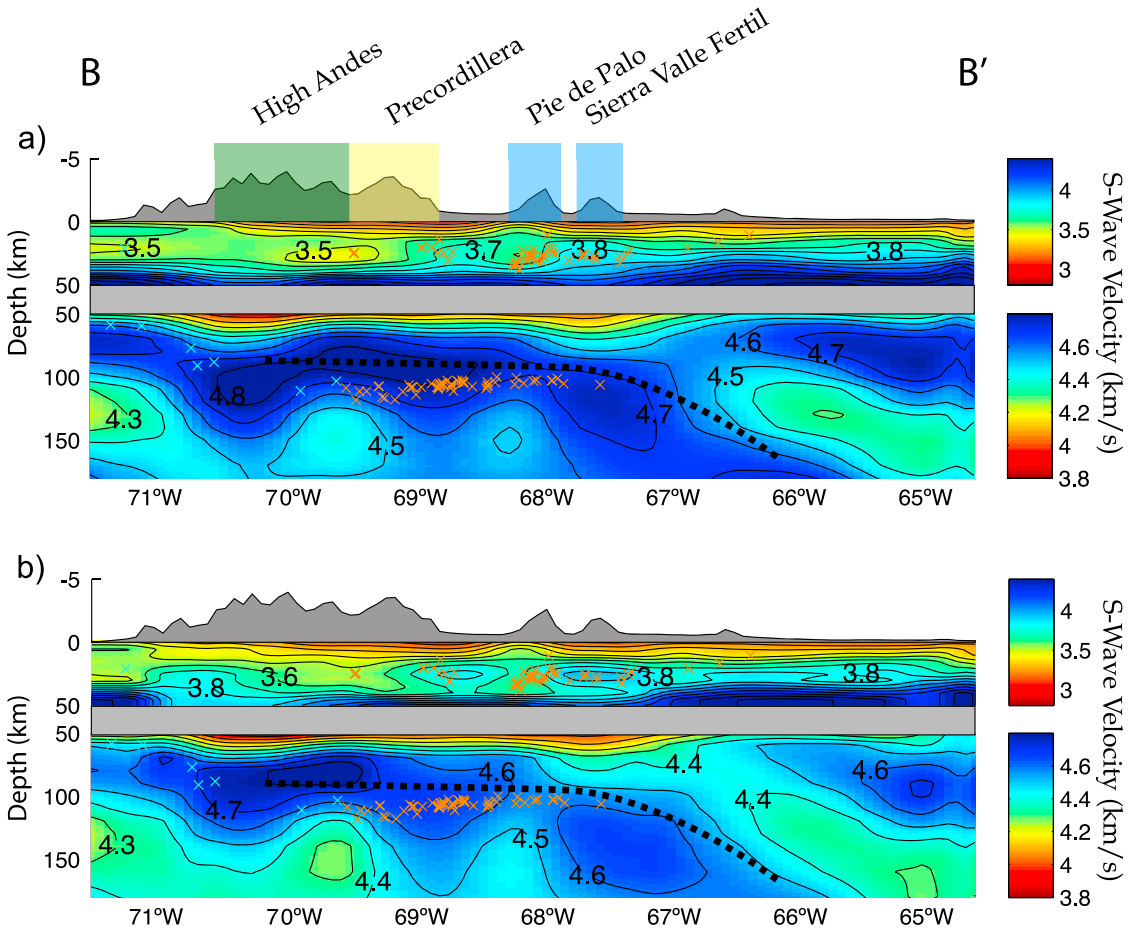

Figure 12. Cross section B-B′ calculated (see location in Figure 1) using (a) a constant velocity initial model and (b) a variable starting model with a gradational Moho. Contour interval is 0.1 km/s. Orange x's are earthquakes locations from Linkimer et al. (manuscript in preparation, 2011). Light-blue x's are earthquake locations from the EHB catalog from 1960 to 2007 (EHB Bulletin, http://www.isc.ac.uk, International Seismological Centre, 2009] within 0.1 degrees of the cross section. Dashed line shows the top of the slab using the slab contours from Linkimer et al. (manuscript in preparation, 2011) and assuming the top of the Benioff zone is 15 km beneath the top of the slab [*Gans et al.*, 2011]. Variable smoothing is used to display cross sections in the crust and mantle in order to observe features in each.

low shear-velocities (<3.3 km/s) are observed in the upper crust beneath the eastern half of the high Andes and the area to their east. These low velocities are likely associated with the active arc and the Payenia volcanic province. The Payenia volcanic province, located to the east of the active arc, is relatively recent (<2 Ma) and is believed to be associated with extension and the emplacement of asthenosphere caused by an increase in slab dip [*Kay et al.*, 2006; *Ramos and Folguera*, 2009, 2011]. The Triassic Cuyo basin [*Uliana et al.*, 1989, 1995] is also located in the same region as the Payenia volcanic province and is another viable explanation for these low upper-crustal velocities. Crustal thickness varies significantly across the region ranging from 60 km thick beneath the arc to 40 km thick in the back-arc [*Gilbert et al.*, 2006]. Though surface waves are not very sensitive to seismic discontinuities, there is a decrease in the depth of the 4.2 km/s velocity contour from west to east, consistent with thick crust beneath the high Andes and thinner crust to the east.

[30] Within the upper mantle, we are able to image the slab and mantle wedge. The slab is observed as a high shear-velocity body (>4.6 km/s) that extends from 60 to 130 km depth at 71°W and dips to the east. The eastward dip of the slab is also visible in map view at 34.5°S as a high-velocity body that shifts eastward with increasing depth between 80 and 165 km and is located at a depth of ~100 km beneath the active arc (Figure 10). The high velocities observed within the normally dipping slab suggest that the oceanic mantle is dry relative to the flat slab and that fluids associated with it and the active arc are confined to the oceanic crust. The oceanic crust of the subducting slab would likely appear as a low-velocity zone at the top of the slab but cannot be imaged here given the wavelength of the surface waves that are sensitive to upper mantle depths, although it has been identified using receiver functions [*Gans et al.*, 2011]. The location of the slab correlates with earthquake locations (USGS PDE catalog) (Figure 11) and has roughly the same ~25°–30° dip as measured by *Fuenzalida et al.* [1992], further affirming its location. Based on slab thickness measurements made in the Atlantic, Pacific and Indian oceans [*Zhang and Lay*, 1999] and assuming a 40–50 Ma

age of the slab at the trench, the subducting oceanic lithosphere should be approximately 60–70 km thick in the region, which is generally consistent with our measurements. Immediately above and to the east of the high velocity body interpreted as the subducting slab, we observe a low-velocity region (<4.3 km/s). This anomaly is visible in map view at depths from 60 to 100 km (Figure 10) and is interpreted as asthenosphere emplaced due to corner flow and the inferred slab rollback. Dependent on starting model, shear velocities in this region are less than 4.0 or 4.1 km/s, which agrees with average back-arc shear velocities calculated in island arc settings [*Wiens and Smith*, 2003].

[31] Cross-section B-B′, in Figure 12, runs parallel to the relative Nazca-South American plate motion and along the region of flattest subduction (Figure 1) at an azimuth of ∼30° northeast. Within this cross-section we observe consistent velocity patterns regardless of starting model (Figures 12a and 12b). As in the southern cross-section, we focus our interpretation on features that are consistent in the shear velocity inversion regardless of initial model. Within the upper crust velocities correlate with basin structure. We observe high velocities at shallow depths beneath basement-cored uplifts and lows associated with basins, consistent with phase velocity measurements (Figure 9). The most prominent features within this area are the Sierra Pie de Palo and the Bermejo basin (Figures 6 and 9). Sierra Pie de Palo, has a large high velocity crustal root that appears to extend down into the mid-crust (Figure 12). This high velocity root and crustal seismicity (Linkimer et al., manuscript in preparation, 2011) suggest that the range bounding thrusts extend down to at least 15 km depth. The Bermejo basin, located northeast of the Sierra Pie de Palo, is the lowest velocity feature observed in the 8 km depth slice, which is consistent with it being a ∼10 km thick sediment filled foreland basin [*Allmendinger et al.*, 1990]. The low-velocity feature associated with the Bermejo basin is considerably larger longitudinally than the surface expression of the basin. The eastward extent of this low-velocity zone can be explained by the smoothing of the Bermejo and Marayes low-velocity zones into one large low-velocity features (Figure 6). To the west there is evidence that the Bermejo basin initially extended to 69°W [*Cardozo and Jordan*, 2001], and has been broken up by deformation related to the Precordillera. The sediment associated with the original extent of the basin can explain the westward extent of the low-velocities observed. The Jocoli foreland basin lies to the south of the Sierra Pie de Palo and exhibits low velocities as well, consistent with previous estimates that suggest a basin thickness of ∼5 km [*Vergés et al.*, 2007].

[32] We observe lower velocities in the mid-crust beneath the high-Andes than are observed beneath the Sierras Pampeanas, possibly related to the transition from the Cuyania into the Pampia terrane or to variations in crustal lithology. The upper mantle of the upper plate is generally fast (>4.6 km/s) west of 68°W, consistent with *Wagner et al.* [2006, 2008]. Based on the depth of the 4.2 km/s velocity contour, eastward thinning of the crust is also observed. The slab is imaged as a region of variable shear wave velocities (4.4–4.6 km/s) immediately beneath the zone of concentrated seismicity. From west to east, the slab transitions at 68°W from a high velocity zone (>4.6 km/s) with pockets of low velocities (<4.6 km/s), to a high velocity region (>4.6 km/s) with no associated low-velocity zones. There is a slightly lower velocity zone (<4.4 km/s) immediately above and to the east of the slab as the angle of subduction steepens at ∼67.5°W. The velocities are not as low as those associated with corner flow to the south and are consistent with either cooling asthenosphere or hydrated lithospheric mantle. A high velocity region (>4.5 km/s) is observed at the base of the crust beneath the Sierras de Córdoba, extending eastward from the western edge of where our model possesses adequate resolution to ∼66°W and to depths of ∼110 km depth. The location of this high velocity zone is consistent with the presence of cratonic lithosphere associated with the Rio de la Plata Craton. In map view, east of 68°S and north of ∼33°S at depths of 120 to 140 km, there is a strong spatial correlation between earthquake locations and an ENE-WSW running high velocity body (>4.7 km/s) (Figure 10). We interpret this as SSE dipping slab representing the transition from flat to normal-angle subduction.

5. Discussion

5.1. Flat-Slab and Upper Mantle Velocities

[33] In the northern part of the study area, where the slab is flat, we interpret our slab and upper mantle shear wave velocity measurements in the context of slab serpentinization, dehydration, and subsequent hydration of the overlying mantle. West of 68°W there is a body of high shear velocities (>4.7 km/s) located between ∼60 and 100 km depth underlain locally by lower velocities (<4.5 km/s) (Figure 12). We interpret the high velocity material as cold-dry continental lithosphere above ∼80 km depth (dashed line in Figure 12), which has been previously identified by body wave tomography [*Wagner et al.*, 2005, 2006, 2008] and the lower velocity material as serpentinized oceanic lithosphere within the subducting slab. These localized low-velocity zones within the slab exhibit an eastward decrease in amplitude. Serpentinite is formed by the hydration of oceanic mantle prior to subduction and is identified seismically by low P- and S- wave velocities and a high Vp/Vs ratio. As the slab subducts, serpentinite becomes unstable at higher temperature and pressure conditions and dehydrates releasing water into overlying mantle. As water leaves the slab, the slab becomes a higher velocity feature, while velocities in the overlying mantle decrease as the mantle absorbs the water released from the slab [*Hacker et al.*, 2003b]. The observed eastward increase in slab and decrease in overlying mantle shear velocities observed in the flat-slab region are consistent with this pattern. Unfortunately, this technique does not allow us to determine the Vp/Vs ratio, which would further test our interpretation.

[34] Serpentinization of the slab mantle lithosphere is common in subduction zones [e.g., *Peacock*, 2001; *Hacker et al.*, 2003b] and is believed to occur at spreading centers, at the outer rise of subduction zones, and along fracture zones. Within this region, the Nazca plate is formed at the fast spreading East Pacific Rise (∼15 cm/yr) and Chile Rise (∼5 cm/year) [*Klitgord et al.*, 1973; *DeMets et al.*, 2010]. Little serpentinization of the mantle lithosphere is believed to occur at fast spreading centers, making spreading center hydration unlikely for the Nazca Plate in this region. However, outer rise extension and fractures associated with the formation of the Juan Fernandez Ridge could enable hydration of the upper mantle

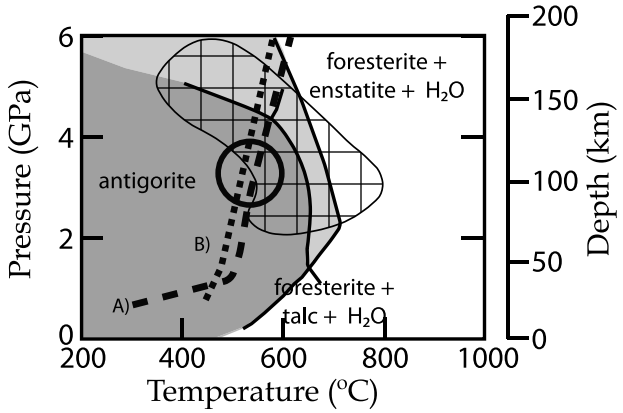

Figure 13. Phase diagram for antigorite modified from *Peacock* [2001], showing P/T paths for the oceanic mantle 20 km beneath the top of the slab from (line A) *English et al.* [2003] (long dashed line) and (line B) *Gutscher et al.* [2000a] (short dashed line). Cross-hatched area is the typical P/T conditions for intermediate depth lower-plane seismicity. Gray shading is the area of antigorite stability. Light gray is antigorite stability from *Ulmer and Trommsdorff* [1995] and *Bose and Navrotsky* [1998], dark gray is stable region from the previous two and *Wunder and Schreyer* [1997]. Circled area is the estimated P-T conditions for 20 km beneath the top of the slab during flat-slab subduction at 100 km depth.

within the slab. Offshore at 30°S there is significant evidence for extensive serpentinization of the Nazca plate based on seismic tomography and earthquake locations [*Kopp et al.*, 2004; *Fromm et al.*, 2006]. Offshore active source seismic work along the Juan Fernandez Ridge shows low P wave velocities in the oceanic mantle extending to at least a depth of 6 km beneath the oceanic Moho [*Kopp et al.*, 2004], indicative of serpentinization of the upper oceanic mantle. Further, the locations of aftershocks from an outer-rise earthquake in 2001 [*Fromm et al.*, 2006; *Clouard et al.*, 2007], suggest that this large outer-rise earthquake in the Nazca plate ruptured at least 20 km beneath the oceanic Moho. Given the fractured nature of the slab along the Juan Fernandez ridge, it is likely that water is penetrating deep within the slab in this region as well.

[35] Serpentinization of the oceanic mantle is typically associated with the creation of an additional plane of seismicity commonly referred to as a "double Benioff zone," that would accompany one plane in the crust of the oceanic lithosphere [*Peacock*, 2001; *Hacker et al.*, 2003b]. Within the Pampean flat-slab region only one plane of seismicity is observed (Linkimer et al., manuscript in preparation, 2011), implying that either seismicity is only occurring in the oceanic crust or within the slab mantle. Receiver function images of the subducting oceanic crust and earthquake locations show that seismicity is concentrated ~20 km beneath the top of the subducting slab, which is well within the oceanic mantle lithosphere [*Alvarado et al.*, 2009; *Gans et al.*, 2011; Linkimer et al., manuscript in preparation, 2011].

[36] Seismicity in the oceanic mantle is commonly attributed to dehydration embrittlement caused by the dehydration reaction of antigorite [*Kirby et al.*, 1996]. Antigorite is the serpentine mineral stable to the greatest pressure/temperature (PT) conditions, which reacts to form forsterite + enstatite + H_2O [*Peacock*, 2001; *Dobson et al.*, 2002; *Hacker et al.*, 2003a]. Using pressure-temperature conditions calculated from thermal modeling of flat-slab subduction [*Gutscher et al.*, 2000a; *English et al.*, 2003] we plot the PT path for the upper oceanic mantle (20 km beneath the top of the slab) in the Pampean flat-slab region on a phase diagram for antigorite [*Peacock*, 2001] (Figure 13). This plot shows that the PT conditions at which earthquakes occur within the flat slab mantle align with the PT conditions where serpentinite dehydration takes place (lines A and B Figure 13). Earthquakes associated with dehydration embrittlement are believed to occur due to the buildup of fluid pressure within the rock, allowing for brittle failure in high P-T conditions [*Raleigh and Paterson*, 1965; *Meade and Jeanloz*, 1991]. The lack of seismicity in the flat-slab crust can be explained by either an early onset or delay in the basalt to eclogite transition. Modeling by *van Hunen et al.* [2002] suggests that ridge subduction may delay this transition to pressures as great as 6 GPa, which corresponds to depths of ~180 km, which is significantly deeper than the flat slab in this region. Modeling by *English et al.* [2003], shows that a 40–50 million year old flat slab at 90 km depth can contain up 1% water where it begins to dip steeply. These modeling results suggest that amphibole becomes unstable as the slab initially subducts and that lawsonite and chlorite are stable throughout the flat slab zone and become unstable as the slab resumes steeper subduction. This implies that dehydration embrittlement in the crust occurs as the slab initially subducts and the slab releases water aseismically as lawsonite and chlorite break down at greater depth. These results offer an explanation for the lack of seismicity within the crust of the Nazca slab where it lies nearly horizontally at ~100 km depth.

[37] The low-velocity regions observed within the flat slab, exhibit an eastward increase in velocity, with shear velocities of 4.3–4.5 km/s observed beneath the high Cordillera and 4.5–4.7 km/s beneath the Sierras Pampeanas where seismicity ceases. We interpret this gradational eastward increase in shear wave velocities to be indicative of slab dewatering as serpentinite becomes unstable and dehydrates, releasing water, which migrates out of the slab into the overlying mantle. This increase in slab S-wave velocity correlates with an eastward decrease in shear velocities in the overlying lithospheric mantle, which transitions from higher values (4.6–4.8 km/s) beneath the high Cordillera to ~4.4–4.5 km/s beneath the central Sierras Pampeanas. These velocities correspond roughly to calculated shear velocities of 4.87 km/s for a dry (70% forsterite and 30% enstatite) mantle and 4.30 km/s for a wet (60% forsterite 20% enstatite and 20% serpentinite) mantle [*Hacker and Abers*, 2004]. The high mantle velocities observed beneath the Andes suggest that water is not immediately escaping the slab. Possible mechanisms for slab dewatering include fluid flow along high-permeability regions [*Hacker et al.*, 2003b], the hydrofracturing of rock along preexisting fractures, and the hydrofracturing of rock in the direction of least compressive stress [*Davies*, 1999]. We expect that the slab bending associated with the transition from a normal angle of subduction to a flat geometry places the upper part of the slab under compression, closing fractures and decreasing the permeability of the top of the slab, which would inhibit all of the above mechanisms for fluid flow. This would result in trapped water within the slab even after serpentinite dehydrates, possibly explaining the thickness

of the observed low-velocity layer. As the slab flattens out, the top of the slab is no longer under compression allowing it to release fluids into the mantle above it. The few focal mechanisms calculated where the slab dip is transitioning from a normal to flat suggest compression while focal mechanisms calculated once it has assumed a flat geometry are largely normal, consistent with this hypothesis [*Pardo et al.*, 2002] (also Global CMT Catalog). Work by *Hasegawa and Sacks* [1981] and *Schneider and Sacks* [1987] on the Peruvian flat slab region, which lies to the north of the study area, show a significant change in stress as the subducting slab flattens. They attribute this to slab pull forces along the edges of the flat slab, but acknowledge that slab bending may impact the stress state of the slab. Regardless of the cause, this shift in stress orientation would likely affect the permeability of the subducting plate, impacting dehydration. When the slab bends to resume a typical angle of subduction, the bending of the slab puts the upper part of the slab into greater tension, allowing the last of the water to escape and the cessation of seismicity.

[38] Lower shear wave velocities are observed in the upper mantle beneath the Sierras Pampeanas from 66°W to 68°W and likely represents hydrated continental lithosphere. At a depth of 40–70 km, antigorite is stable at temperatures less than 650°C [*Ulmer and Trommsdorff*, 1995] and the wet solidus for peridotite is ~825°C [*Grove et al.*, 2006], which suggests that the material could possibly be partially serpentinized mantle or peridotite and free water. While these temperatures are lower than modeled temperatures for continental lithosphere in a flat-slab subduction zone [*Gutscher et al.*, 2000a; *van Hunen et al.*, 2002; *English et al.*, 2003], none of these models incorporate the adjacent Rio de la Plata cratonic lithosphere, whose thickness could prevent asthenosphere to flow into the area above the slab and further refrigerate this portion of mantle, which would inhibit volcanism. The lack of volcanism where normal-angle subduction resumes can also be explained by compression of the Sierras Pampeanas preventing magma from reaching the surface [*Booker et al.*, 2004].

[39] We image a high S-wave velocity zone in the mantle beneath the northeastern Sierras de Córdoba, interpreted to be cratonic lithosphere. The location and thickness of the cratonic lithosphere agrees with S-wave receiver function measurements showing ~125 km thick lithosphere beneath the western Córdoba Range [*Heit et al.*, 2008]. Between the subducting slab and the cratonic lithosphere we observe a low-velocity (<4.4 km/s) region. These velocities are consistent with the presence of a thin dipping layer of asthenosphere or hydrated mantle lithosphere between the slab and continental lithosphere. The location of this low-velocity zone correlates with magnetotelluric measurements, which show a low resistivity zone extending down to depths greater than 400 km [*Booker et al.*, 2004]. Estimates of heat flow from the spectral analysis of magnetic anomalies suggest increased heat flow in the region [*Ruiz and Introcaso*, 2004] where this low-velocity zone intersects the crust, which suggests that the low-velocity zone may be asthenosphere. The absence of significant slab seismicity, possibly related to slab dehydration, beneath this low-velocity zone also supports this hypothesis. However, the subduction related geochemical signature of the young (7.9–4.5 Ma) Pocho volcanics [*Kay and Gordillo*, 1994], located within the Sierras de Córdoba (Figure 6), suggests that at least some lithospheric hydration has occurred within the region. While both options are viable explanations for this feature we prefer to interpret these velocities as lithosphere hydrated by the aseismic release of the remaining water from the slab as it resumes a steep angle of subduction.

5.2. Slab Buoyancy

[40] Numerous ideas have been proposed to explain flat-slab subduction. Possible hypotheses include a high rate of convergence, young slab age, increased slab buoyancy due to overthickened oceanic crust, the hydration of the mantle wedge, slab suction forces, and the hydration of the oceanic slab mantle [e.g., *Stevenson and Turner*, 1977; *Tovish et al.*, 1978; *Pilger*, 1981; *Cross and Pilger*, 1982; *McGeary et al.*, 1985; *Cloos*, 1993; *Gutscher et al.*, 2000b; *van Hunen et al.*, 2002; *Kopp et al.*, 2004; *van Hunen et al.*, 2004; *Guillaume et al.*, 2009; *Skinner and Clayton*, 2010; *Gans et al.*, 2011]. While recent receiver function work in the region suggests that the oceanic crust is moderately overthickened and contributes to the buoyancy of the slab, it is unlikely that this provides all of the necessary buoyancy to maintain flat-slab subduction [*Gans et al.*, 2011]. We propose that the hydration of the slab plays a role in maintaining flat-slab subduction within this region. At 2.5 GPa, corresponding to a depth near 100 km, and 500°C, antigorite has a density of 2654 kg/m^3 [*Hacker and Abers*, 2004]. Assuming a slab density of 3330 kg/m^3 and an asthenosphere density of 3300 kg/m^3 [*Tassara et al.*, 2006], serpentinization of at least 5% of the subducting oceanic lithosphere would cause the slab to no longer be negatively buoyant. While 5% serpentinization is unlikely for the whole slab, partial serpentinization of the upper 20 km of the slab and an overthickened crust could provide the necessary buoyancy to maintain flat-slab subduction. S-wave receiver functions calculated for the region suggest thinner subducting lithosphere in the flat-slab region than to the south [*Heit et al.*, 2008]. This thinning is potentially related to volcanism associated with the Juan Fernandez Ridge and could further reduce the degree of serpentinization necessary to maintain flat slab subduction. This positive buoyancy of the slab would be reduced as antigorite dehydrates and water is released allowing the slab to resume a normal angle of subduction. The serpentinization of the slab would have the added effect of reducing slab strength allowing it more readily bend into a flat geometry.

6. Conclusions

[41] We calculated shear wave velocities for the Pampean flat-slab region using Rayleigh wave phase velocities determined from ambient-noise tomography and from earthquake-generated surface waves employing the two-plane wave approach. Combining these two methods allows for much more detailed analysis of crust and upper-mantle structure than either individual method could provide. Results show that upper-crustal velocities are primarily dependent on lithology and the distribution of volcanism and basins. The mid-crust exhibits an eastward increase in velocities, possibly related to terrane boundaries or to thinning crust. Though surface wave inversions do not have a high sensitivity to sharp seismic discontinuities (i.e., the Moho), crustal thickness estimates for the region do reflect the eastward decrease in Moho depth observed using receiver functions, regional surface waves, and

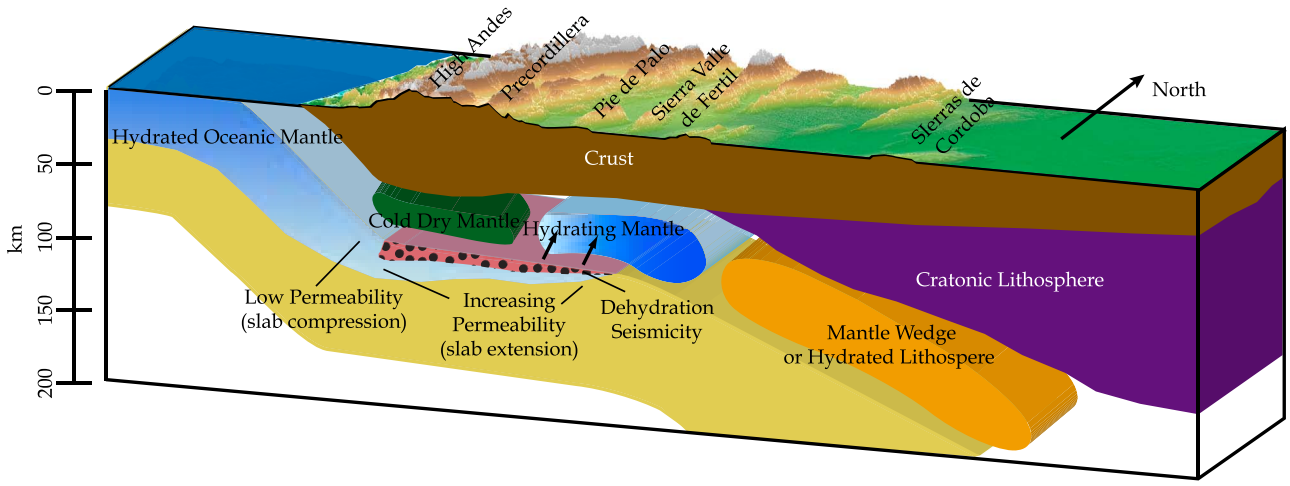

Figure 14. Summary diagram showing our interpretation of flat-slab S-wave velocities along cross section B-B′ in Figure 1.

Pn arrivals [*Fromm et al.*, 2004; *Alvarado et al.*, 2005; *Gilbert et al.*, 2006; *Gans et al.*, 2011]. Regional shear wave velocities for the region also provide new insight into the role of water in flat-slab subduction as shown in Figure 14. These results suggest that the oceanic mantle is hydrated and serpentinized due to fracturing in the crust associated with the Juan Fernandez Ridge. This hydration possibly increases the buoyancy of the subducting slab and weakens it allowing it to assume a flat geometry. As the slab subducts to the east, it dewaters, resulting in increased seismicity due to dehydration embrittlement. The cessation of seismicity at 67.5°W may correspond to the removal of serpentinite and likely the limit of slab dewatering. This would increase the density of the slab and allow it to subduct more steeply into the mantle. The presence of a low-velocity zone above the slab as it steepens east of 66.5°W may be indicative of the slab retaining a small amount of water, which is then released aseismically at depth or may represent cooling asthenosphere. While this model is able to account for some of the increased buoyancy necessary for flat-slab subduction and better explain the role of water in this process, it is increasingly clear that there is not one definitive cause of flat-slab subduction, which instead relies on an interplay of numerous factors.

[42] **Acknowledgments.** Thanks go to Christine Gans and Lepolt Linkimer for their help with this research, to Noel Barstow for her work during the deployment of the SIEMBRA seismometers, and to Arthur Snoke and Erdinc Saygin for their insightful reviews of this manuscript. We acknowledge the support of the Incorporated Research Institutions for Seismology (IRIS) and the PASSCAL Instrument Center for their assistance with the SIEMBRA, CHARGE and ESP seismic deployments. The seismic instruments for CHARGE and SEIMBRA were provided by the PASSCAL Instrument Center (NSF Cooperative Agreement EAR-0552316). We also appreciate the assistance provided by the Instituto Nacional de Prevención Sísmica, Argentina. This research was supported by the National Science Foundation (EAR-0510966, EAR-0738935, EAR-0739001 and EAR-0651540). Figures 1, 2, 6 and 14, S2, S3 and S4 were made using Generic Mapping Tools [*Wessel and Smith*, 1998]. Topography in maps is from *Lindquist et al.* [2004].

References

Allmendinger, R. W., D. Figueroa, D. Snyder, J. Beer, C. Mpodozis, and B. L. Isacks (1990), Foreland shortening and crustal balancing in the Andes at 30°S latitude, *Tectonics*, *9*(4), 789–809, doi:10.1029/TC009i004p00789.

Alvarado, P., S. Beck, G. Zandt, M. Araujo, and E. Triep (2005), Crustal deformation in the south-central Andes backarc terranes as viewed from regional broad-band seismic waveform modelling, *Geophys. J. Int.*, *163*(2), 580–598, doi:10.1111/j.1365-246X.2005.02759.x.

Alvarado, P., S. Beck, and G. Zandt (2007), Crustal structure of the south central Andes Cordillera and backarc region from regional waveform modelling, *Geophys. J. Int.*, *170*(2), 858–875, doi:10.1111/j.1365-246X.2007.03452.x.

Alvarado, P., M. Pardo, H. Gilbert, S. Miranda, M. Anderson, M. Saez, and S. Beck (2009), Flat-slab subduction and crustal models for the seismically active Sierras Pampeanas region of Argentina, in *Backbone of the Americas: Shallow Subduction, Plateau Uplift, and Ridge and Terrane Collision*, edited by S. M. Kay, V. Ramos and W. R. Dickinson, pp. 261–278, Geol. Soc. of Am., Boulder, Colo., doi:10.1130/2009.1204(12).

Anderson, M., P. Alvarado, G. Zandt, and S. Beck (2007), Geometry and brittle deformation of the subducting Nazca Plate, Central Chile and Argentina, *Geophys. J. Int.*, *171*(1), 419–434, doi:10.1111/j.1365-246X.2007.03483.x.

Astini, R. A., J. L. Benedetto, and N. E. Vaccari (1995), The early Paleozoic evolution of the Argentine Precordillera as a Laurentian rifted, drifted, and collided terrane: A geodynamic model, *Geol. Soc. Am. Bull.*, *107*(3), 253–273, doi:10.1130/0016-7606(1995)107<0253:TEPEOT>2.3.CO;2.

Barmin, M. P., M. H. Ritzwoller, and A. L. Levshin (2001), A fast and reliable method for surface wave tomography, *Pure Appl. Geophys.*, *158*(8), 1351–1375, doi:10.1007/PL00001225.

Baumont, D. (2002), Lithospheric structure of the central Andes based on surface wave dispersion, *J. Geophys. Res.*, *107*(B12), 2371, doi:10.1029/2001JB000345.

Bensen, G. D., M. H. Ritzwoller, M. P. Barmin, A. L. Levshin, F. Lin, M. P. Moschetti, N. M. Shapiro, and Y. Yang (2007), Processing seismic ambient noise data to obtain reliable broad band surface wave dispersion measurements, *Geophys. J. Int.*, *169*(3), 1239–1260, doi:10.1111/j.1365-246X.2007.03374.x.

Bensen, G. D., M. H. Ritzwoller, and N. M. Shapiro (2008), Broadband ambient noise surface wave tomography across the United States, *J. Geophys. Res.*, *113*, B05306, doi:10.1029/2007JB005248.

Bissig, T., A. H. Clark, and J. K. W. Lee (2002), Cerro de Vidrio rhyolitic dome: Evidence for Late Pliocene volcanism in the central Andean flat-slab region, Lama-Veladero district, 29°20′S, San Juan Province, Argentina, *J. S. Am. Earth Sci.*, *15*(5), 571–576, doi:10.1016/S0895-9811(02)00077-9.

Booker, J. R., A. Favetto, and M. C. Pomposiello (2004), Low electrical resistivity associated with plunging of the Nazca flat slab beneath Argentina, *Nature*, *429*(6990), 399–403, doi:10.1038/nature02565.

Bose, K., and A. Navrotsky (1998), Thermochemistry and phase equilibria of hydrous phases in the system MgO-SiO_2–H_2O: Implications for volatile transport to the mantle, *J. Geophys. Res.*, *103*(B5), 9713–9719, doi:10.1029/98JB00506.

Cahill, T., and B. Isacks (1992), Seismicity and shape of the subducted Nazca plate, *J. Geophys. Res.*, *97*(B12), 17,503–17,529, doi:10.1029/92JB00493.

Cardozo, N., and T. Jordan (2001), Causes of spatially variable tectonic subsidence in the Miocene Bermejo foreland basin, Argentina, *Basin Res.*, *13*(3), 335–357, doi:10.1046/j.0950-091x.2001.00154.x.

Cloos, M. (1993), Lithospheric buoyancy and collisional orogenesis: Subduction of oceanic plateaus, continental margins, island arcs, spreading

ridges, and seamounts, *Geol. Soc. Am. Bull.*, *105*(6), 715, doi:10.1130/0016-7606(1993)105<0715:LBACOS>2.3.CO;2.
Clouard, V., J. Campos, A. Lemoine, A. Perez, and E. Kausel (2007), Outer rise stress changes related to the subduction of the Juan Fernandez Ridge, central Chile, *J. Geophys. Res.*, *112*, B05305, doi:10.1029/2005JB003999.
Coney, P. J., and S. J. Reynolds (1977), Cordilleran Benioff zones, *Nature*, *270*, 403–406, doi:10.1038/270403a0.
Cross, T. A., and R. Pilger Jr. (1982), Controls of subduction geometry, location of magmatic arcs, and tectonics of arc and back-arc regions, *Geol. Soc. Am. Bull.*, *93*(6), 545–562, doi:10.1130/0016-7606(1982)93<545:COSGLO>2.0.CO;2.
Davies, J. H. (1999), The role of hydraulic fractures and intermediate-depth earthquakes in generating subduction-zone magmatism, *Nature*, *398*(6723), 142–145, doi:10.1038/18202.
DeMets, C., R. G. Gordon, and D. F. Argus (2010), Geologically current plate motions, *Geophys. J. Int.*, *181*(1), 1–80, doi:10.1111/j.1365-246X.2009.04491.x.
Dickinson, W. R., and W. S. Snyder (1978), Plate tectonics of the Laramide orogeny, *Mem. Geol. Soc. Am.*, *151*, 355–366.
Dobson, D. P., P. G. Meredith, and S. A. Boon (2002), Simulation of subduction zone seismicity by dehydration of serpentine, *Science*, *298* (5597), 1407–1410, doi:10.1126/science.1075390.
English, J. M., S. T. Johnston, and K. Wang (2003), Thermal modelling of the Laramide orogeny: Testing the flat-slab subduction hypothesis, *Earth Planet. Sci. Lett.*, *214*(3–4), 619–632, doi:10.1016/S0012-821X(03)00399-6.
Forsyth, D., and A. Li (2005), Array analysis of two-dimensional variations in surface wave phase velocity and azimuthal anisotropy in the presence of multipathing interference, in *Seismic Earth: Array Analysis of Broadband Seismograms*, *Geophys. Monogr. Ser.*, vol. 157, edited by A. Levander and G. Nolet, pp. 81–97, AGU, Washington, D. C., doi:10.1029/157GM06.
Forsyth, D., S. Webb, L. Dorman, and Y. Shen (1998), Phase velocities of Rayleigh waves in the MELT experiment on the East Pacific Rise, *Science*, *280*(5367), 1235–1238, doi:10.1126/science.280.5367.1235.
Friedrich, A., F. Kruger, and K. Klinge (1998), Ocean-generated microseismic noise located with the Grafenberg array, *J. Seismol.*, *2*(1), 47–64, doi:10.1023/A:1009788904007.
Fromm, R., G. Zandt, and S. L. Beck (2004), Crustal thickness beneath the Andes and Sierras Pampeanas at 30°S inferred from Pn apparent phase velocities, *Geophys. Res. Lett.*, *31*, L06625, doi:10.1029/2003GL019231.
Fromm, R., P. Alvarado, S. L. Beck, and G. Zandt (2006), The April 9, 2001 Juan Fernandez Ridge (M_w 6.7) tensional outer-rise earthquake and its aftershock sequence, *J. Seismol.*, *10*(2), 163–170, doi:10.1007/s10950-006-9013-3.
Fuenzalida, A., M. Pardo, A. Cisternas, L. Dorbath, C. Dorbath, D. Comte, and E. Kausel (1992), On the geometry of the Nazca Plate subducted under central Chile (32–34.5°S) as inferred from microseismic data, *Tectonophysics*, *205*(1–3), 1–11, doi:10.1016/0040-1951(92)90413-Z.
Gans, C. R., S. L. Beck, G. Zandt, H. Gilbert, P. Alvarado, M. Anderson, and L. Linkimer (2011), Continental and oceanic crustal structure of the Pampean flat slab region, western Argentina, using receiver function analysis: New high resolution results, *Geophys. J. Int.*, *186*(1), 45–58, doi:10.1111/j.1365-246X.2011.05023.x.
Gilbert, H. J., S. Beck, and G. Zandt (2006), Lithospheric and upper mantle structure of central Chile and Argentina, *Geophys. J. Int.*, *165*(1), 383–398, doi:10.1111/j.1365-246X.2006.02867.x.
Gimenez, M. E., M. P. Martínez, and A. Introcaso (2000), A crustal model based mainly on gravity data in the area between the Bermejo Basin and the Sierras de Valle Fertil, Argentina, *J. S. Am. Earth Sci.*, *13*(3), 275–286, doi:10.1016/S0895-9811(00)00012-2.
Grove, T. L., N. Chatterjee, S. W. Parman, and E. M. Èdard (2006), The influence of H_2O on mantle wedge melting, *Earth Planet. Sci. Lett.*, *249*(1–2), 74–89, doi:10.1016/j.epsl.2006.06.043.
Guillaume, B., J. Martinod, and N. Espurt (2009), Variations of slab dip and overriding plate tectonics during subduction: Insights from analogue modelling, *Tectonophysics*, *463*(1–4), 167–174, doi:10.1016/j.tecto.2008.09.043.
Gutscher, M. A. (2002), Andean subduction styles and their effect on thermal structure and interplate coupling, *J. S. Am. Earth Sci.*, *15*(1), 3–10, doi:10.1016/S0895-9811(02)00002-0.
Gutscher, M. A., R. Maury, J. P. Eissen, and E. Bourdon (2000a), Can slab melting be caused by flat subduction?, *Geology*, *28*(6), 535, doi:10.1130/0091-7613(2000)28<535:CSMBCB>2.0.CO;2.
Gutscher, M. A., W. Spakman, H. Bijwaard, and E. R. Engdahl (2000b), Geodynamics of flat subduction: Seismicity and tomographic constraints from the Andean margin, *Tectonics*, *19*(5), 814–833, doi:10.1029/1999TC001152.
Hacker, B. R., and G. A. Abers (2004), Subduction Factory 3: An Excel worksheet and macro for calculating the densities, seismic wave speeds, and H_2O contents of minerals and rocks at pressure and temperature, *Geochem. Geophys. Geosyst.*, *5*, Q01005, doi:10.1029/2003GC000614.
Hacker, B. R., G. A. Abers, and S. M. Peacock (2003a), Subduction factory 1. Theoretical mineralogy, densities, seismic wave speeds, and H_2O contents, *J. Geophys. Res.*, *108*(B1), 2029, doi:10.1029/2001JB001127.
Hacker, B. R., S. M. Peacock, G. A. Abers, and S. D. Holloway (2003b), Subduction factory 2. Are intermediate-depth earthquakes in subducting slabs linked to metamorphic dehydration reactions, *J. Geophys. Res.*, *108*(B1), 2030, doi:10.1029/2001JB001129.
Hasegawa, A., and I. S. Sacks (1981), Subduction of the Nazca plate beneath Peru as determined from seismic observations, *J. Geophys. Res.*, *86*(B6), 4971–4980, doi:10.1029/JB086iB06p04971.
Heit, B., X. Yuan, M. Bianchi, F. Sodoudi, and R. Kind (2008), Crustal thickness estimation beneath the southern central Andes at 30°S and 36°S from *S* wave receiver function analysis, *Geophys. J. Int.*, *174*(1), 249–254, doi:10.1111/j.1365-246X.2008.03780.x.
Herrmann, R. B. (Ed.) (1987), Computer programs in seismology, report, 183 pp., St. Louis Univ., St. Louis, Mo.
Introcaso, A., M. C. Pacino, and H. Fraga (1992), Gravity, isostasy and Andean crustal shortening between latitudes 30 and 35°S, *Tectonophysics*, *205*(1–3), 31–48, doi:10.1016/0040-1951(92)90416-4.
Jischke, M. C. (1975), On the dynamics of descending lithospheric plates and slip zones, *J. Geophys. Res.*, *80*(35), 4809–4813, doi:10.1029/JB080i035p04809.
Jordan, T. E., and R. W. Allmendinger (1986), The Sierras Pampeanas of Argentina: A modern analogue of Rocky Mountain foreland deformation, *Am. J. Sci.*, *286*(10), 737–764, doi:10.2475/ajs.286.10.737.
Jordan, T. E., B. L. Isacks, R. W. Allmendinger, J. A. Brewer, V. A. Ramos, and C. J. Ando (1983), Andean tectonics related to geometry of subducted Nazca plate, *Geol. Soc. Am. Bull.*, *94*(3), 341, doi:10.1130/0016-7606(1983)94<341:ATRTGO>2.0.CO;2.
Kay, S. M., and C. E. Gordillo (1994), Pocho volcanic rocks and the melting of depleted continental lithosphere above a shallowly dipping subduction zone in the central Andes, *Contrib. Mineral. Petrol.*, *117*(1), 25–44, doi:10.1007/BF00307727.
Kay, S. M., and C. Mpodozis (2001), Central Andean ore deposits linked to evolving shallow subduction systems and thickening crust, *GSA Today*, *11*(3), 4–9.
Kay, S. M., and C. Mpodozis (2002), Magmatism as a probe to the Neogene shallowing of the Nazca plate beneath the modern Chilean flat-slab, *J. S. Am. Earth Sci.*, *15*(1), 39–57, doi:10.1016/S0895-9811(02)00005-6.
Kay, S. M., V. Maksaev, R. Moscoso, C. Mpodozis, C. Nasi, and C. E. Gordillo (1988), Tertiary Andean magmatism in Chile and Argentina between 28°S and 33°S: Correlation of magmatic chemistry with a changing Benioff zone, *J. S. Am. Earth Sci.*, *1*(1), 21–38, doi:10.1016/0895-9811(88)90013-2.
Kay, S. M., W. M. Burns, P. Copeland, and O. Mancilla (2006), Upper Cretaceous to Holocene magmatism and evidence for transient Miocene shallowing of the Andean subduction zone under the northern Neuquen Basin, in *Evolution of an Andean Margin: A Tectonic and Magmatic View From the Andes to the Neuquén Basin (35°–39°S lat)*, *GSA Spec. Pap.*, vol. 407, edited by S. M. Kay and V. Ramos, pp. 19–60, Geol. Soc. of Am., Boulder, Colo., doi:10.1130/2006.2407(02).
Kendrick, E., M. Bevis, and R. Smalley (2003), The Nazca–South America Euler vector and its rate of change, *J. S. Am. Earth Sci.*, *16*(2), 125–131, doi:10.1016/S0895-9811(03)00028-2.
Kennett, B. L. N., and E. R. Engdahl (1991), Traveltimes for global earthquake location and phase identification, *Geophys. J. Int.*, *105*(2), 429–465, doi:10.1111/j.1365-246X.1991.tb06724.x.
Kirby, S., E. R. Engdahl, and R. Denlinger (1996), Intermediate-depth intraslab earthquakes and arc volcanism as physical expressions of crustal and uppermost mantle metamorphism in subducting slabs, in *Subduction Top to Bottom*, *Geophys. Monogr. Ser.*, vol. 96, edited by G. E. Bebout et al., pp. 195–214, AGU, Washington, D. C.
Klitgord, K. D., J. D. Mudie, P. A. Larson, and J. A. Grow (1973), Fast seafloor spreading on the Chile Ridge, *Earth Planet. Sci. Lett.*, *20*(1), 93–99, doi:10.1016/0012-821X(73)90144-1.
Kopp, H., E. R. Flueh, C. Papenberg, and D. Klaeschen (2004), Seismic investigations of the O'Higgins Seamount Group and Juan Fernandez Ridge: Aseismic ridge emplacement and lithosphere hydration, *Tectonics*, *23*, TC2009, doi:10.1029/2003TC001590.
Larson, M. A., J. A. Snoke, and D. E. James (2006), S-wave velocity structure, mantle xenoliths and the upper mantle beneath the Kaapvaal craton, *Geophys. J. Int.*, *167*(1), 171–186, doi:10.1111/j.1365-246X.2006.03005.x.
Lindquist, K. G., K. Engle, D. Stahlke, and E. Price (2004), Global topography and bathymetry grid improves research efforts, *Eos Trans. AGU*, *85*(19), 186, doi:10.1029/2004EO190003.
McGeary, S., A. Nur, and Z. Ben-Avraham (1985), Spatial gaps in arc volcanism: The effect of collision or subduction of oceanic plateaus, *Tectonophysics*, *119*(1–4), 195–221, doi:10.1016/0040-1951(85)90039-3.

Meade, C., and R. Jeanloz (1991), Deep-focus earthquakes and recycling of water into the Earth's mantle, *Science*, *252*(5002), 68–72, doi:10.1126/science.252.5002.68.

Mitchell, B. J. (1995), Anelastic structure and evolution of the continental crust and upper mantle from seismic surface wave attenuation, *Rev. Geophys.*, *33*(4), 441–462, doi:10.1029/95RG02074.

Moschetti, M. P., M. H. Ritzwoller, and N. M. Shapiro (2007), Surface wave tomography of the western United States from ambient seismic noise: Rayleigh wave group velocity maps, *Geochem. Geophys. Geosyst.*, *8*, Q08010, doi:10.1029/2007GC001655.

Pardo, M., D. Comte, and T. Monfret (2002), Seismotectonic and stress distribution in the central Chile subduction zone, *J. S. Am. Earth Sci.*, *15*(1), 11–22, doi:10.1016/S0895-9811(02)00003-2.

Peacock, S. M. (2001), Are the lower planes of double seismic zones caused by serpentine dehydration in subducting oceanic mantle?, *Geology*, *29*(4), 299–302, doi:10.1130/0091-7613(2001)029<0299:ATLPOD>2.0.CO;2.

Pilger, R. E. X. H., Jr. (1981), Plate reconstructions, aseismic ridges, and low-angle subduction beneath the Andes, *Geol. Soc. Am. Bull.*, *92*(7), 448–456, doi:10.1130/0016-7606(1981)92<448:PRARAL>2.0.CO;2.

Raleigh, C. B., and M. S. Paterson (1965), Experimental deformation of serpentinite and its tectonic implications, *J. Geophys. Res.*, *70*(16), 3965–3985, doi:10.1029/JZ070i016p03965.

Ramos, V. A. (2004), Cuyania, an exotic block to Gondwana: Review of a historical success and the present problems, *Gondwana Res.*, *7*(4), 1009–1026, doi:10.1016/S1342-937X(05)71081-9.

Ramos, V. A. (2010), The Grenville-age basement of the Andes, *J. S. Am. Earth Sci.*, *29*(1), 77–91, doi:10.1016/j.jsames.2009.09.004.

Ramos, V. A., and M. A. Basei (1997a), Gondwanan, Perigondwanan, and exotic terranes of southern South America, paper presented at South American Symposium on Isotope Geology, Univ. Nac. de Colombia, Sao Paulo, Brazil.

Ramos, V. A., and M. T. Basei (1997b), The basement of Chilenia: An exotic continental terrane to Gondwana during the Early Paleozoic, paper presented at Symposium on Terrane Dynamics, Univ. of Canterbury, Christchurch, New Zealand.

Ramos, V. A., and A. Folguera (2009), Andean flat-slab subduction through time, *Geol. Soc. London Spec. Publ.*, *327*(1), 31–54, doi:10.1144/SP327.3.

Ramos, V. A., and A. Folguera (2011), Payenia volcanic province in the Southern Andes: An appraisal of an exceptional Quaternary tectonic setting, *J. Volcanol. Geotherm. Res.*, *201*(1–4), 53–64, doi:10.1016/j.jvolgeores.2010.09.008.

Ramos, V., T. Jordan, R. Allmendinger, C. Mpodozis, S. M. Kay, J. Cortés, and M. Palma (1986), Paleozoic terranes of the central Argentine-Chilean Andes, *Tectonics*, *5*(6), 855–880, doi:10.1029/TC005i006p00855.

Ramos, V. A., S. M. Kay, R. S. Harmon, and C. W. Rapela (1991), Triassic rifting and associated basalts in the Cuyo basin, central Argentina, in *Andean Magmatism and Its Tectonic Setting*, edited by R. S. Harmon and C. W. Rapela, pp. 79–91, Geol. Soc. of Am., Boulder, Colo.

Ramos, V. A., E. O. Cristallini, and D. J. Pérez (2002), The Pampean flat-slab of the central Andes, *J. S. Am. Earth Sci.*, *15*(1), 59–78, doi:10.1016/S0895-9811(02)00006-8.

Ramos, V. A., G. Vujovich, R. Martino, and J. Otamendi (2010), Pampia: A large cratonic block missing in the Rodinia supercontinent, *J. Geodyn.*, *50*(3–4), 243–255, doi:10.1016/j.jog.2010.01.019.

Rapela, C. W., R. J. Pankhurst, C. Casquet, E. Baldo, J. Saavedra, C. Galindo, and C. M. Fanning (1998), The Pampean Orogeny of the southern proto-Andes: Cambrian continental collision in the Sierras de Córdoba, *Geol. Soc. Spec. Publ.*, *142*(1), 181–217, doi:10.1144/GSL.SP.1998.142.01.10.

Roux, P., K. G. Sabra, P. Gerstoft, W. A. Kuperman, and M. C. Fehler (2005), *P* waves from cross-correlation of seismic noise, *Geophys. Res. Lett.*, *32*, L19303, doi:10.1029/2005GL023803.

Ruiz, F., and A. Introcaso (2004), Curie point depths beneath Precordillera Cuyana and Sierras Pampeanas obtained from spectral analysis of magnetic anomalies, *Gondwana Res.*, *7*(4), 1133–1142, doi:10.1016/S1342-937X(05)71089-3.

Sacks, I. S. (1983), The subduction of young lithosphere, *J. Geophys. Res.*, *88*(B4), 3355–3366, doi:10.1029/JB088iB04p03355.

Schneider, J. F., and I. S. Sacks (1987), Stress in the contorted Nazca plate beneath southern Peru from local earthquakes, *J. Geophys. Res.*, *92*(B13), 13,887–13,902, doi:10.1029/JB092iB13p13887.

Shapiro, N. M., M. Campillo, L. Stehly, and M. H. Ritzwoller (2005), High-resolution surface-wave tomography from ambient seismic noise, *Science*, *307*(5715), 1615, doi:10.1126/science.1108339.

Skinner, S. M., and R. W. Clayton (2010), An evaluation of proposed mechanisms of slab flattening in central Mexico, *Pure Appl. Geophys.*, *168*, 1461–1474, doi:10.1007/s00024-010-0200-3.

Snoke, J. A., and D. E. James (1997), Lithospheric structure of the Chaco and Paraná Basins of South America from surface-wave inversion, *J. Geophys. Res.*, *102*(B2), 2939–2951, doi:10.1029/96JB03180.

Stachnik, J. C., K. Dueker, D. L. Schutt, and H. Yuan (2008), Imaging Yellowstone plume-lithosphere interactions from inversion of ballistic and diffusive Rayleigh wave dispersion and crustal thickness data, *Geochem. Geophys. Geosyst.*, *9*, Q06004, doi:10.1029/2008GC001992.

Stern, C. R. (2004), Active Andean volcanism: Its geologic and tectonic setting, *Rev. Geol. Chile*, *31*(2), 161–206, doi:10.4067/S0716-02082004000200001.

Stevenson, D. J., and J. S. Turner (1977), Angle of subduction, *Nature*, *270*, 334–336, doi:10.1038/270334a0.

Tassara, A., H. J. Gotze, S. Schmidt, and R. Hackney (2006), Three-dimensional density model of the Nazca plate and the Andean continental margin, *J. Geophys. Res.*, *111*, B09404, doi:10.1029/2005JB003976.

Thomas, W. A., and R. A. Astini (1996), The Argentine Precordillera: A traveler from the Ouachita embayment of North American Laurentia, *Science*, *273*(5276), 752, doi:10.1126/science.273.5276.752.

Thomas, W. A., and R. A. Astini (2003), Ordovician accretion of the Argentine Precordillera terrane to Gondwana: A review, *J. S. Am. Earth Sci.*, *16*(1), 67–79, doi:10.1016/S0895-9811(03)00019-1.

Tovish, A., G. Schubert, and B. P. Luyendyk (1978), Mantle flow pressure and the angle of subduction: Non-Newtonian corner flows, *J. Geophys. Res.*, *83*(B12), 5892–5898, doi:10.1029/JB083iB12p05892.

Uliana, M., K. Biddle, J. Cerdan, A. Tankard, and H. Balkwill (1989), Mesozoic extension and the formation of Argentine sedimentary basins, *AAPG Mem.*, *46*, 599–613.

Uliana, M. A., M. E. Arteaga, L. Legarreta, J. J. Cerdan, and G. O. Peroni (1995), Inversion structures and hydrocarbon occurrence in Argentina, in *Basin Inversion*, edited by J. G. Buchanan and P. G. Buchanan, pp. 211–233, Geol. Soc. London, London, doi:10.1144/GSL.SP.1995.088.01.13.

Ulmer, P., and V. Trommsdorff (1995), Serpentine stability to mantle depths and subduction-related magmatism, *Science*, *268*(5212), 858–861, doi:10.1126/science.268.5212.858.

van Hunen, J., A. P. van den Berg, and N. J. Vlaar (2002), On the role of subducting oceanic plateaus in the development of shallow flat subduction, *Tectonophysics*, *352*(3–4), 317–333, doi:10.1016/S0040-1951(02)00263-9.

van Hunen, J., A. P. van den Berg, and N. J. Vlaar (2004), Various mechanisms to induce present-day shallow flat subduction and implications for the younger Earth: A numerical parameter study, *Phys. Earth Planet. Inter.*, *146*(1–2), 179–194, doi:10.1016/j.pepi.2003.07.027.

Vergés, J., V. A. Ramos, A. Meigs, E. Cristallini, F. H. Bettini, and J. M. Cortés (2007), Crustal wedging triggering recent deformation in the Andean thrust front between 31°S and 33°S: Sierras Pampeanas-Precordillera interaction, *J. Geophys. Res.*, *112*, B03S15, doi:10.1029/2006JB004287.

Vlaar, N. J., and M. J. R. Wortel (1976), Lithospheric aging, instability and subduction, *Tectonophysics*, *32*(3–4), 331–351, doi:10.1016/0040-1951(76)90068-8.

Vujovich, G. I., C. R. van Staal, and W. Davis (2004), Age constraints on the tectonic evolution and provenance of the Pie de Palo Complex, Cuyania composite terrane, and the Famatinian Orogeny in the Sierra de Pie de Palo, San Juan, Argentina, *Gondwana Res.*, *7*(4), 1041–1056, doi:10.1016/S1342-937X(05)71083-2.

Wagner, L., S. Beck, and G. Zandt (2005), Upper mantle structure in the south central Chilean subduction zone (30° to 36°S), *J. Geophys. Res.*, *110*, B01308, doi:10.1029/2004JB003238.

Wagner, L., S. Beck, G. Zandt, and M. N. Ducea (2006), Depleted lithosphere, cold, trapped asthenosphere, and frozen melt puddles above the flat slab in central Chile and Argentina, *Earth Planet. Sci. Lett.*, *245*(1–2), 289–301, doi:10.1016/j.epsl.2006.02.014.

Wagner, L., M. L. Anderson, J. M. Jackson, S. L. Beck, and G. Zandt (2008), Seismic evidence for orthopyroxene enrichment in the continental lithosphere, *Geology*, *36*(12), 935, doi:10.1130/G25108A.1.

Warren, L. M., J. A. Snoke, and D. E. James (2008), S-wave velocity structure beneath the High Lava Plains, Oregon, from Rayleigh-wave dispersion inversion, *Earth Planet. Sci. Lett.*, *274*(1–2), 121–131, doi:10.1016/j.epsl.2008.07.014.

Wessel, P., and W. H. F. Smith (1998), New, improved version of Generic Mapping Tools released, *Eos Trans. AGU*, *79*, 579, doi:10.1029/98EO00426.

Wiens, D. A., and G. P. Smith (2003), Seismological constraints on structure and flow patterns within the mantle wedge, in *Inside the Subduction Factory*, *Geophys. Monogr. Ser.*, vol. 138, edited by J. Eiler, pp. 59–81, AGU, Washington, D. C., doi:10.1029/138GM05.

Wunder, B., and W. Schreyer (1997), Antigorite: High-pressure stability in the system MgO-SiO_2–H_2O (MSH), *Lithos*, *41*(1–3), 213–227, doi:10.1016/S0024-4937(97)82013-0.

Yáñez, G. A., C. R. Ranero, R. von Huene, and J. Díaz (2001), Magnetic anomaly interpretation across the southern central Andes (32°–34°S): The role of the Juan Fernández Ridge in the late Tertiary evolution of the margin, *J. Geophys. Res.*, *106*(B4), 6325–6345, doi:10.1029/2000JB900337.

Yáñez, G. A., J. Cembrano, M. Pardo, C. Ranero, and D. Selles (2002), The Challenger-Juan Fernández-Maipo major tectonic transition of the Nazca-Andean subduction system at 33–34°S: Geodynamic evidence and implications, *J. S. Am. Earth Sci.*, *15*(1), 23–38, doi:10.1016/S0895-9811(02)00004-4.

Yang, Y., and D. W. Forsyth (2006), Regional tomographic inversion of the amplitude and phase of Rayleigh waves with 2 D sensitivity kernels, *Geophys. J. Int.*, *166*(3), 1148–1160, doi:10.1111/j.1365-246X.2006.02972.x.

Yang, Y., and D. W. Forsyth (2008), Attenuation in the upper mantle beneath Southern California: Physical state of the lithosphere and asthenosphere, *J. Geophys. Res.*, *113*, B03308, doi:10.1029/2007JB005118.

Yang, Y., M. H. Ritzwoller, A. L. Levshin, and N. M. Shapiro (2007), Ambient noise Rayleigh wave tomography across Europe, *Geophys. J. Int.*, *168*(1), 259–274, doi:10.1111/j.1365-246X.2006.03203.x.

Yang, Y., M. H. Ritzwoller, F. C. Lin, M. P. Moschetti, and N. M. Shapiro (2008), Structure of the crust and uppermost mantle beneath the western United States revealed by ambient noise and earthquake tomography, *J. Geophys. Res.*, *113*, B12310, doi:10.1029/2008JB005833.

Zhang, Y. S., and T. Lay (1999), Evolution of oceanic upper mantle structure, *Phys. Earth Planet. Inter.*, *114*(1–2), 71–80, doi:10.1016/S0031-9201(99)00047-3.

Zhou, Y., F. A. Dahlen, and G. Nolet (2004), Three dimensional sensitivity kernels for surface wave observables, *Geophys. J. Int.*, *158*(1), 142–168, doi:10.1111/j.1365-246X.2004.02324.x.

Zhou, Y., G. Nolet, F. A. Dahlen, and G. Laske (2006), Global upper-mantle structure from finite-frequency surface-wave tomography, *J. Geophys. Res.*, *111*, B04304, doi:10.1029/2005JB003677.